ADA278824

Effects of Winglets on a First-Generation Jet Transport Wing

VII—Sideslip Effects on Winglet Loads and Selected Wing Loads at Subsonic Speeds for a Full-Span Model

Robert R. Meyer, Jr.,
and Peter F. Covell

Ames Research Center
Dryden Flight Research Facility
Edwards, California

SUMMARY

The effect of sideslip on winglet loads and selected wing loads was investigated at high and low subsonic Mach numbers. The investigation was conducted in two separate wind tunnel facilities, using two slightly different 0.035-scale full-span models. Results are presented which indicate that, in general, winglet loads as a result of sideslip are analogous to wing loads caused by angle of attack. The center-of-pressure locations on the winglets are somewhat different than might be expected for an analogous wing. The spanwise center of pressure for a winglet tends to be more inboard than for a wing. The most notable chordwise location is a forward center-of-pressure location on the winglet at high sideslip angles. The noted differences between a winglet and an analogous wing are the result of the influence of the wing on the winglet.

INTRODUCTION

Winglets, described in reference 1, are intended to provide substantially greater reductions in drag caused by lift at subsonic speeds than reductions obtained with simple wingtip extensions that have bending moments at the wing-fuselage juncture essentially equal to those produced by the winglets. The National Aeronautics and Space Administration (NASA) has conducted extensive experimental investigations on the effects of winglets for representative jet transport wings at high subsonic Mach numbers (refs. 1 to 8). For example, the winglets developed in reference 3 for a first-generation jet transport wing lowered the induced drag near design lift coefficients by about 20 percent with a resulting increase in wing lift-drag ratio of about 9 percent at the design Mach number of 0.78. The improvements were more than twice as great as those achieved with a simple wingtip extension with essentially equal wing-bending moments at the wing-fuselage juncture.

As a result of these indicated gains in performance, NASA and the U.S. Air Force (USAF) conducted a joint winglet flight research and demonstration program on USAF KC-135A aircraft (ref. 9). To support the flight research program, extensive wind tunnel investigations were conducted on semispan and full-span models of the KC-135A aircraft. Performance, loads, stability and control, and buffet data were obtained over the aircraft operational envelope.

Semispan model tests of the KC-135A aircraft are described in references 3 to 5. Results of these tests indicated that the gains associated with the use of a lower winglet on the KC-135A aircraft were considered marginal. Therefore, for simplification, the lower winglet was not used in the design for the KC-135A application.

This paper, which is one of a series (refs. 3 to 8), presents results obtained on low-speed and high-speed full-span models of the USAF KC-135A aircraft from two separate wind tunnel entries. The investigation was conducted to determine the effects of sideslip on wing and winglet loads. Results are presented for a takeoff configuration with and without aileron deflections and for a representative cruise configuration.

Low-speed data were obtained for Mach 0.30 and through an angle of sideslip range from -12° to 12°. High-speed data are presented for Mach 0.70, 0.78, 0.90, and 0.95 and for angles of sideslip of -5°, 0°, and 5°. Some data were obtained for a constant Reynolds number of $1.0 \times 10^6/m$ ($3.3 \times 10^6/ft$). The angle of attack varied from approximately -13° to 17°. The high subsonic speed tests were conducted in the NASA Langley 8-Foot Transonic Pressure Tunnel, and low-speed tests were conducted in the NASA Langley High-Speed 7- by 10-Foot Tunnel.

NOMENCLATURE

The results presented in this report are referenced to the stability-axis system for the aircraft longitudinal aerodynamic characteristics. Wing and winglet force and moment data have been reduced to

conventional coefficient form based on the geometry of the reference wing or winglet planform, respectively. (See fig. 1 for winglet sign convention.) All dimensional values are given in both the International System of Units (SI, ref. 10) and U.S. Customary Units. Computer indentifiers are given in parentheses.

b wing span, 138.7 cm (54.6 in)

b' exposed semispan of wing, cm (in)

c (C)   local section chord of reference wing or winglet panel

c_{av} (CAV)   average chord of reference wing planform, S/b, 19.47 cm (7.66 in)

c_{av_w} average chord of reference winglet planform, s_w/h, 4.01 cm (1.68 in)

c_{B_W} winglet bending moment coefficient obtained from integration of winglet load distribution, $\dfrac{\text{bending moment}}{q_\infty s_w h}$,

$$\int_0^1 \left(\frac{z}{h}\right)\left(\frac{c}{c_{av_w}}\right)(c_n)\ d\left(\frac{z}{h}\right)$$

C_L total lift coefficient, $\dfrac{\text{lift}}{q_\infty S}$

c_m (CM)   section pitching-moment coefficient obtained from integration of section pressure distributions, $\dfrac{\text{moment}}{q_\infty c}$, about 0.25c,

$$\int_0^1 \left(c_{p\ell} - c_{pu}\right)\left(\frac{x}{c}\right)\ d\left(\frac{x}{c}\right)$$

c_{N_W} winglet normal-force coefficient obtained from integration of spanwise load distribution, $\dfrac{\text{normal force}}{q_\infty S}$,

$$\int_0^1 \left(\frac{c}{c_{av_w}}\right)(c_n)\ d\left(\frac{z}{h}\right)$$

c_n (CN)   section normal-force coefficient obtained from integration of section pressure distribution, $\dfrac{\text{section normal force}}{q_\infty c}$,

$$\int_0^1 \left(c_{p\ell} - c_{pu}\right)\ d\left(\frac{x}{c}\right)$$

c_p (CP)   pressure coefficient, $\dfrac{P - P_\infty}{q_\infty}$

c_t tip chord of basic wing, cm (in)

C_{T_W} winglet torque coefficient obtained from integration of spanwise moment distribution, $\dfrac{\text{torque}}{q_\infty S_w c_{av}}$, about 0.25c_{av},

$$\int_0^1 \left(c_{m_{c_{av_w}}}\right)\left(\frac{c}{c_{av}}\right)^2\ d\left(\frac{z}{h}\right)$$

h winglet span, 9.96 cm (3.92 in)

i_t horizontal tail incidence, deg

M Mach number

M_∞ free-stream Mach number

P static pressure, kPa (lb/ft^2)

P_∞ free-stream static pressure, kPa (lb/ft^2)

q dynamic pressure, kPa (lb/ft^2)

q_∞ free-stream dynamic pressure, kPa (lb/ft^2)

Re Reynolds number

S reference wing planform area, 0.270 m^2 (2.91 ft^2)

s_w reference winglet planform area, 0.0043 m^2 (0.047 ft^2)

x (X)   chordwise distance from leading edge, positive aft, cm (in)

2

$\bar{y}$ semispan distance from fuselage centerline, cm (in)

z   vertical distance, positive upward, used for coordinate of airfoil and vertical distance along winglet reference planform, cm (in)

α angle of attack, deg

β angle of sideslip, positive nose left, (left winglet aft), deg

$\delta_{a,L}$ left aileron deflection, positive for trailing edge down, deg

$\delta_{a,R}$ right aileron deflection, positive for trailing edge down, deg

δ_f flap deflection, positive for trailing edge down, deg

η exposed wing semispan station, y/b', or winglet semispan station, z/h

Subscripts:

c.p.   center of pressure

w   winglet

ℓ lower

u   upper

APPARATUS AND PROCEDURES

Test Facilities

The investigation discussed in this paper was conducted in two NASA Langley wind tunnel test facilities. The low-speed data (free-stream Mach number $(M_\infty) = 0.30$)) were obtained in the NASA Langley High-Speed 7- by 10-Foot Tunnel, which is a continuous, single-return atmospheric tunnel with a closed rectangular test section. The high-speed data $(M_\infty > 0.70)$ were obtained in the NASA Langley 8-Foot Transonic Pressure Tunnel, which is a continuous, single-return tunnel with a slotted, rectangular test section. The longitudinal slots in the floor and ceiling of the test section reduce tunnel wall interference and allow relatively large models to be tested through the subsonic speed range. Controls are available to permit independent variation of Mach number, stagnation pressure, temperature, and dewpoint. A more detailed description of both tunnels is found in reference 11.

Model Descriptions

Two wind tunnel models with different fuselages were used in this investigation. The low-speed $(M_\infty = 0.30)$ model was a 0.035-scale version of a KC-135A aircraft, while the high-speed $(M_\infty > 0.70)$ model consisted of a 0.035-scale version of KC-135A aircraft wing panels mounted on a generalized fuselage. A comparison of the two model fuselages is shown in figure 2.

Wing

The basic wing of the KC-135A aircraft model has 7° dihedral and 2° incidence at the root chord and has no geometric twist. An outboard wing airfoil section is shown in figure 3, and coordinates are presented in table 1. The wing thickness ratio varies nonlinearly from 15 percent at the wing-fuselage juncture to 9 percent at the trailing-edge break station and then remains constant to the tip. The trapezoidal planform of the basic wing extended to the fuselage centerline (fig 4(a)) has a sweep of 35° at the quarter chord, an aspect ratio of 7.0, and taper ratio of 0.35.

The basic planform geometry of the high-speed model wing was identical to that of the low-speed wing; however, some specific differences did exist between the two wings. The low-speed model wing incorporated flaps and ailerons (fig. 4(b)), whereas the high-speed model wing had no flaps or controls. The winglet static pressure orifice tubes on the

low-speed model were routed outside of the wing on the lower surface, while the high-speed wing and winglet pressure tubes were routed inside the wing. Wing static pressure orifices were incorporated only in the high-speed model and were routed internally.

Flaps and Ailerons (Low-Speed Model)

Fixed flaps and outboard ailerons simulating the full-scale configurations were incorporated in the model. Flap deflections could be set at 0°, 30°, and 50°. The available aileron deflections were 0°, ±10°, and ±20°. A drawing of the flaps and ailerons used in this investigation is shown in figure 4(b).

Nacelles

Flowthrough nacelles that had an inlet diameter of 2.90 cm (1.14 in) and an exit diameter of 2.08 cm (0.82 in) were used. The inlet diameter was maintained to approximately 0.66 of the nacelle length and then tapered linearly to the exit.

Winglets

A drawing of the winglet used in this investigation is shown in figure 4(c). The winglet employed an 8-percent-thick general aviation airfoil section shown in figure 4(c); the coordinates are presented in table 2. The winglet used in this investigation is the same as that which had been used in previous full-span KC-135A aircraft investigations (refs. 6, 7, and 8).

The winglet has a span equal to the wingtip chord, a root chord equal to 65 percent of the wingtip chord, a leading-edge sweep of 38°, a taper ratio of 0.32, and an aspect ratio of 2.33. The planform area of each winglet is 1.6 percent of the trapezoidal planform area of the basic wing. The winglet is canted outboard 15° from the vertical (75° dihedral) and toed out 4° (leading edge outboard) relative to the fuselage centerline. The winglet is untwisted and therefore has constant negative geometric incidence across its span. To smooth the transition from the wing to the winglet, fillets were added to the inside corners at those junctures, and the outside corners were rounded.

Low-Speed Fuselage

The fuselage contours closely simulated the full-scale fuselage shape, with the exception of the aft fuselage area. An enlargement of this area was necessitated by the sting mounting apparatus. Drawings of the low-speed model are shown in figure 4, and photographs of the model are shown in figure 5.

High-Speed Fuselage

A tailless generalized research fuselage was used to represent the actual KC-135A aircraft fuselage in this investigation. Drawings of the high-speed model are presented in figure 6, and photographs of the model are shown in figure 7.

The high-speed fuselage used in this investigation has a maximum diameter of 14.58 cm (5.74 in) and is 125.88 cm (49.56 in) long. The fuselage wetted area is approximately 0.52 m^2 (5.63 ft^2). The fineness ratio of the fuselage is slightly less than those for narrow-body first-generation jet transport aircraft such as the KC-135A.

The wing lower surface was faired into the fuselage to provide a relatively flat bottom region that extended from near the wing leading edge to approximately the trailing edge of the wing. This lower surface fillet did not increase the maximum diameter of the fuselage.

Boundary-Layer Transition

Boundary-layer transition strips were placed on the fuselage, pylons, and

4

nacelles and on both surfaces of the wings, winglets, horizontal tail, and vertical tail. These strips consisted of bands (0.15 cm (0.06 in) wide) of Carborundum[1] grains set in a plastic adhesive. The Carborundum grains and the strip width are sized for the test Mach number on the basis of information in reference 12. The transition strips were applied at conventional locations on all surfaces except the winglet lower surfaces where they were located by the method in reference 13 in an attempt to simulate a full-scale trailing-edge boundary-layer displacement thickness at a Reynolds number based on the mean aerodynamic chord of 40×10^6.

On the fuselage, number 220 grains were applied 3.81 cm (1.50 in) aft of the nose. Number 220 grain transition strips were applied at 5-percent chord on the upper and lower surfaces of the wings, horizontal tail, and vertical tail. Transition strips on the winglets were number 240 grains applied at 5-percent chord on the upper surface and number 220 grains applied at 35-percent chord on the lower surface. The pylons and nacelles had number 240 grain transition strips placed 0.64 cm (0.25 in) from the leading edges.

Measurements

Force and moment data were obtained using a six-component electrical strain-gage balance housed within the fuselage cavity during the investigation. However, this report is oriented toward loads, and only limited reference force data are presented. Complete force and moment results for similar configurations can be obtained in references 6 and 7. Angle of attack was measured by an accelerometer that was housed within the fuselage.

Static pressures were measured in the model sting cavity and at the model base by using differential-pressure trans-

---

[1]Carborundum Co., Niagara Falls, N.Y.

ducers referenced to free-stream static pressures.

The high-speed model incorporated wing chordwise static-pressure orifices in the right wing panel and winglet chordwise static-pressure orifices on the left winglet. Wing chordwise static-pressure orifices were located at the 0.13, 0.26, 0.39, 0.64, 0.82, 0.92, and 0.98 semispan stations (fig. 8(a)). Winglet chordwise static-pressure orifices were located at 0.15 and 0.80 span of winglet (fig. 8(b)). The wing and winglet pressures were measured with pressure scanning valves. The low-speed model incorporated winglet chordwise static-pressure orifices on the left winglet at locations identical to those for the high-speed model with no wing static orifices.

Corrections

The angle of attack of the model was corrected for flow angularity in the 8-foot tunnel test section, but no correction was applied to data obtained from the 7- by 10-foot tunnel. The correction in the 8-foot tunnel was obtained from upright and inverted tests of the baseline wing configuration. No Mach number correction was applied to the data for blockage or tunnel wall effects.

Test Conditions

The test conditions for which data were taken and the corresponding wind tunnel facility in which the data were obtained are presented in table 3.

PRESENTATION OF RESULTS

The results presented in this paper represent data for only those conditions where extensive wing separation did not exist; however, tables 4 and 5 (microfiche supplement) present tabulated pressure coefficient data for all the conditions explored in the experimental investigation. Winglet loads data are summarized in table 6 and were

5

analyzed from the pressure coefficient data contained in tables 4 and 5.

The results of this investigation are presented in the following figures:

DISCUSSION

Full-Span and Semispan Model Considerations

Previous experimental investigations
(refs. 3 to 5) of the effects of winglets
on the KC-135A jet transport aircraft
were primarily concerned with performance
and aerodynamic loads parameters (partic-
ularly wing root bending) at cruise and
second-segment-climb conditions. For
those investigations, a 0.07-scale
semispan model was used to obtain the
highest possible winglet Reynolds number.

The purpose of the investigation dis-
cussed in this paper was to examine the
effects of sideslip on wing and, in par-
ticular, winglet loads, because such data
were not obtainable on the semispan model.
In the investigation two full-span sting-
mounted models were used.

The earlier semispan and present
full-span models were generally tested
at similar combinations of Mach number
and dynamic pressure. However, the
structural properties of each model were
different, and no generalized comparisons
of data have been made between models.

The full-span models were very rigid,
as indicated by the data in figure 9
where results for the high-speed full-
span model near cruise conditions are
shown for dynamic pressures of 25.6 kPa
(534 lb/ft^2) and 40.7 kPa (850 lb/ft^2),
representing a 59-percent increase in
aerodynamic loading. Figure 9 shows very
little difference in the wing span loads
at the increased aerodynamic loading,
indicating rigidity or minimal deflection
(twist) of the full-span model wing under
load.

The semispan model (refs. 3 to 5), on
the other hand, was designed to simulate
full-scale aircraft wing deflections
under load. It is well known that swept-
back flexible wings deflect under load in
a manner to "wash-out" or unload the
wingtip sections. Figure 10 compares
spanwise load distributions for the

7

full-span high-speed model (which is essentially rigid) and the semispan model (ref. 4), which was intended to approximate the full-scale deflections under load. As can be seen from figure 10, the winglets and the outboard portions of the wings are more highly loaded on the full-span model, at least until higher angles of attack (see fig. 10(c) where $\alpha = 5.19°$) where flow separation begins on the full-span model wing before the semispan wing because of higher local angles of attack on the wingtip region of the full-span model. This separation results in lower local loads (c_nc/c_{av}) for the wingtip ($\eta = 0.98$) and winglet of the full-span model. Figure 11 presents pressure distributions on the winglets and two outboard wing stations that correspond to the conditions presented in the span load distributions presented in figure 10. It should be noted that the span location of the wing pressure orifices differ slightly ($\eta = 0.93$ and 0.99 on the semispan model wing and $\eta = 0.92$ and 0.98 on the full-span model wing). Futhermore, the outboard portion of the full-span model wing appears to be at approximately a 2° higher local angle of attack than that indicated from the semispan model. Compare, for example, figure 11(a) where $\alpha = 0.09$ for the full-span model results with figure 11(b) where $\alpha = 2.05$ for those of the semispan model. Of interest in figure 11(c) where $\alpha = 5.17°$ is that trailing-edge separation occurred on the full-span model wingtip ($\eta = 0.92$ and 0.98) and on the inboard portion of the winglet ($\eta = 0.15$ winglet), but not on the semispan model. The separation is so notable that the second upper surface pressure peak on the semispan model wing (at $\eta = 0.99$) caused by the presence of the winglet does not appear in the full-span model pressure distribution. The variations noted in figures 10 and 11 are the probable result of combined aeroelastic and Reynolds number effects, because Reynolds number is doubled on the semispan model.

Because of the observed differences associated with separation of the full-span and semispan models, data analysis

and results presented in this report are for conditions where extensive wing separation did not exist. More complete analysis can be made from the data presented in pressure coefficient form in tables 4 and 5.

Since the loads presented in this report (which have been obtained from the full-scale models) are subject to error in terms of absolute level with respect to the full-span airplane, the reader is cautioned to exercise judgment in the application of the results because of the noted aeroelastic and Reynolds number effects. The trends and incremental values associated with winglets should be of the most interest since they are felt to be representative of those on the full-scale airplane. The data in this report should only be compared with full-scale flight results in terms of incremental values. Because of uncertainties in lift coefficient in flight caused by both trim considerations on the full-scale airplane and the aforementioned Reynolds number and aeroelastic effects, angle of attack was felt to be a more meaningful parameter than lift coefficient by which to present the basic data. As a matter of convenience, figure 12 presents tail-off lift coefficient as a function of angle of attack for the full-span high-speed model. The full-span models do not deflect under load in the same way as a full-scale airplane, and any comparison of the data presented in this report with full-scale results should include adjustments for these effects. One such correction might apply to the local angle of attack at the wingtip.

Representative Wing and Winglet Span Loads

Figures 13 and 14 present representative span load distributions for the right wing panel of the full-span model. These distributions were obtained from tabulated pressure coefficients presented in table 4. Figure 13 presents span load data for near-cruise conditions for

several angles of attack at selected sideslip angles. Figure 14 presents span load data at a selected angle of attack for varying sideslip angles.

Figure 13 shows expected results because loads increase with angle of attack up to tip stall (see fig. 11 for an indication of tip stall) where the tip loads are decreased. Figures 13 and 14 indicate that the wing loads increase over the outboard panel on the forward moving wing as the effective sweep decreases. This effect is particularly evident as shown in the results of figure 14.

Figures 15 to 18 present representative left winglet span load distributions for takeoff and cruise conditions obtained from the tabulated pressure data in tables 4 and 5. These data have been integrated and are summarized in table 6. Because of physical limitations of the model winglet, only two pressure rows were available on the winglets; consequently, only two data points are available to define each winglet span load. It should be noted the winglet span load fairing through two data points is subject to error; however, based on experience gained from references 4 and 5, the fairings are felt to be representative. Representative winglet span loads used for analysis in this report are presented with their respective data fairing. It is interesting to note in figure 16(a) that at large positive angles of sideslip the left winglet span load is "sinusoidal" in nature, similar to that of a twisted wing at low angles of attack. This effect is caused by the combined influence of the wing loading the root of the winglet in an opposite direction of that caused by the relatively high negative angle of attack on the winglet resulting from sideslip.

Winglet Load Characteristics

Figures 19 through 21 present left winglet loads data in the form of normal force, bending-moment, and torsional coefficients as a function of angle of attack at several angles of sideslip for the model in a takeoff configuration (the data were obtained from the values presented in table 4). Figures 22 to 24 are derived from figures 19 to 21 and present left winglet loads as a function of sideslip angle for a constant angle of attack of 4.5°, which is representative of a takeoff condition. Examining the normal force coefficient (c_n) as a function of sideslip angle (β) for several aileron deflections (figs. 22 to 24) depicts the angle of sideslip at which flow separation begins to occur. This angle is defined as the break in the torque coefficient (C_T) and C_N as a function of β curve and is denoted by arrows on figures 22 and 23. Note that for the left winglet, changing the sideslip angle to a more negative value is analogous to increasing the angle of attack on a wing. For a left aileron deflection ($\delta_{a,L}$) of 0° (fig. 22), separation begins at approximately -9° of sideslip. At $\delta_{a,L}$ = 20° (fig. 23), the left winglet begins to separate at approximately -5° of sideslip, and for $\delta_{a,L}$ = -20° (fig. 24), the left winglet did not begin to separate at the maximum sideslip angle for which data were obtained at -12°. These results were expected because at these conditions (α = 4.5° and M_∞ = 0.30) the wing is near stall (see fig. 11 of ref. 6) and aileron deflection would be expected to significantly affect the outboard wing and winglet stall characteristics.

Figures 25 to 28 present left winglet loads for high subsonic speeds as a function of angle of attack for several angles of sideslip (the data were obtained from the values presented in table 5). These results show the expected influence of wing loadings on the winglet loads and stall.

Figures 29 to 31 were obtained from the results of figures 19 to 28 and present winglet spanwise and chordwise center-of-pressure location as a function of angle of sideslip and Mach number. The spanwise and chordwise center-of-pressure locations were obtained by

dividing the winglet bending by the normal force (C_{B_W}/C_{N_W}) and the winglet torque by normal force (C_{T_W}/C_{N_W}), respectively.

It is interesting to note that the chordwise center of pressure generally varies from 5 percent to approximately 30 percent of the average chord. The exception is for $\delta_{a,L} = -20°$ and a sideslip angle in the region of 9.5° (fig. 29), where the center-of-pressure location moves quite far aft. Examination of figure 21 shows that at $\delta_{a,L} = -20°$ and $\beta = 9.7°$ the load (C_{N_W}) is very nearly zero, which explains the large excursion in the center of pressure at these conditions since center of pressure is the torque divided by the normal force (C_{T_W}/C_{N_W}). Other notable conditions are the 5-percent center-of-pressure locations. The left winglet is highly loaded at negative angles of sideslip where the forward center-of-pressure location occurs and could cause high torque conditions on the winglet because of a high load at a forward center-of-pressure location.

The winglet spanwise center-of-pressure location is more inboard than might be expected for a wing; however, results of the method described in reference 14 indicate that the ideal span load distribution from the viewpoint of achieving minimum induced drag for a winglet (nonplanar lifting surface) is linear (nearly triangular) rather than elliptical as it is for a wing. Consequently, the winglet spanwise center-of-pressure location would generally be expected to be more inboard than that for a wing, which results in this paper indicate.

Figure 30 presents winglet spanwise and chordwise center-of-pressure location as a function of angle of sideslip for several high subsonic Mach numbers at an angle of attack of 1°, which is representative of cruise conditions. Figure 31 presents winglet spanwise and chordwise

center-of-pressure location as a function of Mach number for sideslip angles of 0° and ±5°. The center-of-pressure locations are somewhat different than might be expected for an analogous wing, because the flow field around the winglet is strongly influenced by the wing. The noted load differences between a winglet and an analogous wing are the result of the influence of the wing on the winglet.

CONCLUSIONS

The effect of sideslip on winglet loads and selected wing loads of a 0.035-scale model of a first-generation jet transport airplane (U.S. Air Force KC-135A aircraft) was investigated at high and low subsonic Mach numbers. Because of the noted aeroelastic and Reynolds number differences between the full-span wind tunnel model and the full-scale airplane, the reader is cautioned to exercise judgment in the application of the results of this report.

As expected, tip loads on the full-span model wing with winglets increased with angle of attack up to tip stall, where the tip loads decreased. The loads over the outboard portion of the left wing increased with negative sideslip (left wing forward).

Winglet loads as a result of sideslip are analogous to wing loads caused by angle of attack, in that negative sideslip (left winglet forward) increases the loads on the left winglet, while positive sideslip (left wing aft) decreases the left winglet loads. At large positive sideslip (left winglet aft), the left winglet span load is "sinusodial" in nature, similar to that of a twisted wing at low angles of attack. Wing aileron deflection significantly affects the sideslip angle at which separation begins on the winglet.

The center-of-pressure location on the winglets is somewhat different than might be expected for an analogous wing. The spanwise center of pressure for a winglet tends to be more inboard than for

·a wing. The most notable chordwise loca-
tion is a forward center-of-pressure
location on the winglet at high sideslip
angles. The noted differences between a
winglet and an analogous wing are the
result of the influence of the wing on
the winglet.

Ames Research Center
Dryden Flight Research Facility
National Aeronautics and Space
Administration
Edwards, California, July 15, 1983

REFERENCES

1. Whitcomb, Richard T.: A Design
Approach and Selected Wind-Tunnel Results
at High Subsonic Speed for Wing-Tip
Mounted Winglets. NASA TN D-8260, 1976.

2. Flechner, Stuart G; Jacobs, Peter F;
and Whitcomb, Richard T.: A High Sub-
sonic Speed Wind-Tunnel Investigation of
Winglets on a Representative Second-
Generation Jet Transport Wing. NASA
TN D-8264, 1976.

3. Jacobs, Peter F.; Flechner, Stuart
G.; and Montoya, Lawrence C.: Effect of
Winglets on a First-Generation Jet Trans-
port Wing. I — Longitudinal Aerodynamic
Characteristics of a Semispan Model at
Subsonic Speeds. NASA TN D-8473, 1977.

4. Montoya, Lawrence C.; Flechner,
Stuart G.; and Jacobs, Peter F.: Effect
of Winglets on a First-Generation Jet
Transport Wing. II — Pressure and Span-
wise Load Distributions for a Semispan
Model at High Subsonic Speeds. NASA
TN D-8474, 1977.

5. Montoya, Lawrence C.; Jacobs, Peter
F.; and Flechner, Stuart G.: Effect of
Winglets on a First-Generation Jet Trans-
port Wing. III — Pressure and Spanwise
Load Distributions for a Semispan Model
at Mach 0.30. NASA TN D-8478, 1977.

6. Meyer, Robert R., Jr.: Effect of
Winglets on a First-Generation Jet Trans-
port Wing. IV — Stability Character-
istics for a Full-Span Model at Mach 0.30.
NASA TP-1119, 1978.

7. Jacobs, Peter F.: Effect of Winglets
on a First-Generation Jet Transport Wing.
V — Stability Characteristics of a Full-
Span Wing With a Generalized Fuselage at
High Subsonic Speeds. NASA TP-1163, 1978.

8. Flechner, Stuart G.: Effect of Wing-
lets on a First-Generation Jet Transport
Wing. VI — Stability Characteristics For
a Full-Span Model at Subsonic Speeds.
NASA TP-1330, 1979.

9. KC-135 Winglet Program Review. NASA
CP-2211, 1981.

10. Mechtly, E. A.: The International
System of Units — Physical Constants and
Conversion Factors (Sec. Revision). NASA
SP-7012, 1973.

11. Schaefer, William T., Jr.: Charac-
teristics of Major Active Wind Tunnels at
the Langley Research Center. NASA
TM X-1130, 1965.

12. Braslow, Albert L.; and Knox, Eugene
C.: Simplified Method for Determination
of Critical Height of Distributed Rough-
ness Particles for Boundary-Layer Transi-
tion at Mach Numbers from 0 to 5. NACA
TN-4363, 1958.

13. Blackwell, James A., Jr.: Prelim-
inary Study of Effects of Reynolds Number
and Boundary-Layer Transition Location on
Shock-Induced Separation. NASA TN D-5003,
1969.

14. Lundry, J. L.: A Numerical Solution
for the Minimum Induced Drag, and the
Corresponding Loading, of Nonplanar Wings.
McDonnell Douglas Corp. Report DAC-66900,
Mar. 1968.

TABLE 1. — COORDINATES OF TYPICAL OUTBOARD WING SECTION
(Wing section at 2° incidence)

Upper surface		Lower surface	
x/c	z/c	x/c	z/x
0	0	0	0
0.0011	0.0042	0.0020	-0.0054
0.0022	0.0056	0.0035	-0.0063
0.0034	0.0071	0.0061	-0.0073
0.0058	0.0090	0.0092	-0.0081
0.0095	0.0116	0.0201	-0.0097
0.0132	0.0136	0.0391	-0.0116
0.0180	0.0161	0.0631	-0.0139
0.0234	0.0186	0.0950	-0.0168
0.0324	0.0221	0.1016	-0.0174
0.0415	0.0253	0.1445	-0.0212
0.0536	0.0291	0.1826	-0.0245
0.0716	0.0338	0.2235	-0.0284
0.0897	0.0377	0.2597	-0.0314
0.0990	0.0394	0.2950	-0.0341
0.1132	0.0417	0.3326	-0.0366
0.1408	0.0454	0.3726	-0.0391
0.1589	0.0471	0.4276	-0.0418
0.1740	0.0483	0.4690	-0.0429
0.1861	0.0492	0.5110	-0.0433
0.2011	0.0501	0.5560	-0.0430
0.2192	0.0510	0.5967	-0.0424
0.2342	0.0516	0.6386	-0.0414
0.2584	0.0522	0.6818	-0.0406
0.3432	0.0522	0.7243	-0.0397
0.3729	0.0524	0.7620	-0.0389
0.4090	0.0513	0.7951	-0.0381
0.4572	0.0489	0.8308	-0.0377
0.5054	0.0454	0.8662	-0.0371
0.5416	0.0420	0.9029	-0.0363
0.5897	0.0367	0.9392	-0.0358
0.6379	0.0304	0.9790	-0.0348
0.6862	0.0226	0.9999	-0.0350
0.7343	0.0513		
0.7582	0.0108		
0.7823	0.0065		
0.8040	0.0027		
0.8344	-0.0023		
0.8642	-0.0076		
0.8874	-0.0119		
0.9223	-0.0180		
0.9492	-0.0229		
0.9718	-0.0269		
0.9920	-0.0308		
1.0001	-0.0347		

TABLE 2. — AIRFOIL COORDINATES FOR WINGLETS

x/c	z/c	
	Upper surface	Lower surface
0	0	0
0.0020	0.0077	-0.0032
0.0050	0.0119	-0.0041
0.0125	0.0179	-0.0060
0.0250	0.0249	-0.0077
0.0375	0.0296	-0.0090
0.0500	0.0333	-0.0100
0.0750	0.0389	-0.0118
0.1000	0.0433	-0.0132
0.1250	0.0469	-0.0144
0.1500	0.0499	-0.0154
0.1750	0.0525	-0.0161
0.2000	0.0547	-0.0167
0.2500	0.0581	-0.0175
0.3000	0.0605	-0.0176
0.3500	0.0621	-0.0174
0.4000	0.0628	-0.0168
0.4500	0.0627	-0.0158
0.5000	0.0618	-0.0144
0.5500	0.0599	-0.0122
0.5750	0.0587	-0.0106
0.6000	0.0572	-0.0090
0.6250	0.0554	-0.0071
0.6500	0.0533	-0.0052
0.6750	0.0508	-0.0033
0.7000	0.0481	-0.0015
0.7250	0.0451	0.00C4
0.7500	0.0419	0.0C20
0.7750	0.0384	0.0036
0.8000	0.0349	0.0049
0.8250	0.0311	0.0060
0.8500	0.0270	0.0065
0.8750	0.0228	0.0064
0.9000	0.0184	0.0059
0.9250	0.0138	0.0045
0.9500	0.0089	0.0021
0.9750	0.0038	-0.0013
1.0000	-0.0020	-0.0067

TABLE 3. — TEST CONDITIONS AND FACILITIES

M_∞	α, deg	β, deg	$Re \times 10^{-6}$, per m (per ft)	q_∞, kPa (lb/ft²)	$\delta_{a,L}$, deg	δ_f, deg	i_t, deg	Wind tunnel facility, ft size
0.30	-5.5 to 16.0	-12 to 12	0.6 (2.0)	6.0 (125)	0	30	-10	7 x 10
0.30	-5.5 to 16.0	-12 to 12	0.6 (2.0)	6.0 (125)	20	30	-10	7 x 10
0.30	-5.5 to 16.0	-12 to 12	0.6 (2.0)	6.0 (125)	-20	30	-10	7 x 10
0.70	-8.0 to 15.5	0, -5, 5	1.0 (3.3)	23.6 (493)	---	---	---	8
0.70	-8.0 to 5.0	0, -5, 5	1.7 (5.7)	40.7 (850)	---	---	---	8
0.78	-8.0 to 15.5	0, -5, 5	1.0 (3.3)	25.6 (534)	---	---	---	8
0.78	-8.0 to 5.0	0, -5, 5	1.7 (5.2)	40.7 (850)	---	---	---	8
0.90	-8.0 to 16.0	0, -5, 5	1.0 (3.3)	28.1 (587)	---	---	---	8
0.90	-8.0 to 7.0	0, -5, 5	1.6 (4.8)	40.7 (850)	---	---	---	8
0.95	-8.0 to 16.0	0, -5, 5	1.0 (3.4)	29.6 (618)	---	---	---	8
0.95	-8.0 to 10.0	0, -5, 5	1.2 (3.8)	33.9 (707)	---	---	---	8

Tables 4 and 5 are in the microfiche supplement included with this report.

14

TABLE 6. – SUMMARY OF WINGLET LOADS DATA

M_∞	β, deg	α, deg	$\delta_{a,L}$, deg	δ_f, deg	$Re \times 10^{-6}$, per m (per ft)	q_∞, kPa (lb/ft²)	$\eta = 0.15$		$\eta = 0.80$		c_{B_W}	c_{B_W}	c_{D_W}
							c_n	c_m	c_n	c_m			
0.30	-12.20	1.90	20	30	0.6 (2.0)	6.0 (125)	0.997	-0.181	0.546	-0.096	0.827	0.284	0.035
0.30	-12.20	4.33	20	30	0.6 (2.0)	6.0 (126)	1.021	-0.183	0.545	-0.095	0.842	0.288	0.040
0.30	-12.10	6.68	20	30	0.6 (2.0)	6.0 (125)	1.035	-0.056	0.598	-0.100	0.868	0.302	0.130
0.30	-12.00	8.82	20	30	0.6 (2.0)	6.0 (125)	0.801	-0.098	0.568	-0.097	0.704	0.256	0.043
0.30	-9.10	1.70	20	30	0.6 (2.0)	6.1 (127)	1.173	-0.065	0.588	-0.092	0.956	0.322	0.162
0.30	-9.10	4.12	20	30	0.6 (2.0)	6.1 (127)	1.082	-0.165	0.552	-0.097	0.885	0.299	0.067
0.30	-9.00	6.41	20	30	0.6 (2.0)	6.1 (127)	0.937	-0.052	0.548	-0.089	0.788	0.274	0.116
0.30	-9.00	8.63	20	30	0.6 (2.0)	6.1 (128)	0.662	-0.097	0.564	-0.094	0.610	0.232	0.009
0.30	-5.10	1.60	20	30	0.6 (2.0)	6.1 (127)	0.939	-0.032	0.779	-0.040	0.859	0.324	0.127
0.30	-5.10	3.98	20	30	0.6 (2.0)	6.0 (126)	1.027	-0.015	0.573	-0.077	0.855	0.295	0.168
0.30	-5.10	6.26	20	30	0.6 (2.0)	6.0 (126)	0.791	-0.054	0.485	-0.073	0.672	0.236	0.089
0.30	-5.10	8.45	20	30	0.6 (2.0)	6.1 (127)	0.488	-0.080	0.532	-0.071	0.485	0.196	-0.011
0.30	0.20	1.63	20	30	0.6 (2.0)	6.1 (127)	0.710	-0.040	0.519	-0.064	0.628	0.230	0.079
0.30	0.20	3.98	20	30	0.6 (2.0)	6.1 (127)	0.786	-0.030	0.626	-0.053	0.711	0.266	0.099
0.30	0.20	6.28	20	30	0.6 (2.0)	6.1 (127)	0.560	-0.059	0.442	-0.040	0.506	0.189	0.043
0.30	0.20	8.44	20	30	0.6 (2.0)	6.1 (127)	0.313	-0.060	0.442	-0.033	0.342	0.147	-0.019
0.30	5.10	1.58	20	30	0.6 (2.0)	6.1 (127)	0.492	-0.050	0.199	-0.075	0.386	0.125	0.043
0.30	5.10	4.01	20	30	0.6 (2.0)	6.1 (127)	0.585	-0.048	0.356	-0.069	0.496	0.174	0.055
0.30	5.10	6.29	20	30	0.6 (2.0)	6.1 (127)	0.412	-0.058	0.382	-0.053	0.389	0.151	0.007
0.30	5.10	8.49	20	30	0.6 (2.0)	6.1 (127)	0.143	-0.028	0.325	-0.043	0.194	0.094	-0.031
0.30	9.60	1.68	20	30	0.6 (2.0)	6.1 (127)	0.316	-0.056	-0.062	-0.080	0.202	0.047	0.014
0.30	9.60	4.07	20	30	0.6 (2.0)	6.1 (127)	0.428	-0.051	0.117	-0.076	0.319	0.097	0.033
0.30	9.50	6.40	20	30	0.6 (2.0)	6.1 (127)	0.181	-0.017	0.235	-0.064	0.192	0.081	-0.012
0.39	9.50	8.65	20	30	0.6 (2.0)	6.1 (128)	-0.093	0.033	0.219	-0.049	-0.001	0.027	-0.037
0.30	12.20	1.58	20	30	0.6 (2.0)	6.0 (126)	0.205	-0.059	-0.317	-0.059	0.051	-0.026	0.016
0.30	12.20	3.98	20	30	0.6 (2.0)	6.0 (125)	0.326	-0.053	-0.061	-0.071	0.209	0.049	0.022
0.30	12.20	6.41	20	30	0.6 (2.0)	6.0 (126)	-0.065	-0.040	0.140	-0.071	-0.005	0.016	-0.026
0.30	12.20	8.59	20	30	0.6 (2.0)	6.0 (126)	-0.225	-0.069	0.189	-0.057	-0.102	-0.004	-0.044
0.30	-12.20	1.71	-20	30	0.6 (2.0)	6.0 (125)	0.950	-0.031	0.738	-0.109	0.854	0.317	0.171
0.30	-12.20	4.12	-20	30	0.6 (2.0)	6.0 (125)	1.103	-0.037	0.540	-0.088	0.895	0.300	0.107
0.30	-12.10	6.53	-20	30	0.6 (2.0)	6.0 (126)	0.851	-0.024	0.596	-0.096	0.745	0.270	0.073
0.30	-12.10	8.68	-20	30	0.6 (2.0)	6.0 (125)	0.802	-0.047	0.615	-0.106	0.719	0.266	0.075
0.30	-9.10	1.47	-20	30	0.6 (2.0)	6.0 (126)	0.746	-0.034	0.781	-0.043	0.732	0.292	0.113
0.30	-9.10	3.91	-20	30	0.6 (2.0)	6.0 (126)	0.868	-0.015	0.655	-0.094	0.775	0.286	0.084
0.30	-9.00	6.21	-20	30	0.6 (2.0)	6.0 (125)	0.735	-0.021	0.580	-0.090	0.664	0.247	0.015
0.30	-9.00	8.43	-20	30	0.6 (2.0)	6.0 (125)	0.592	-0.053	0.623	-0.103	0.582	0.233	0.041
0.30	-5.10	1.42	-20	30	0.6 (2.0)	6.0 (126)	0.550	-0.036	0.535	-0.058	0.527	0.207	0.070
0.30	-5.10	3.83	-20	30	0.6 (2.0)	6.0 (125)	0.661	-0.026	0.646	-0.047	0.635	0.249	0.048
0.30	-5.10	6.14	-20	30	0.6 (2.0)	6.1 (127)	0.534	-0.031	0.583	-0.026	0.531	0.214	0.002
0.30	-5.10	8.33	-20	30	0.6 (2.0)	6.1 (127)	0.369	-0.050	0.443	-0.036	0.380	0.157	0.007
0.30	0.20	1.45	-20	30	0.6 (2.0)	6.1 (127)	0.318	-0.041	0.200	-0.068	0.272	0.096	0.036
0.30	0.20	3.85	-20	30	0.6 (2.0)	6.1 (127)	0.437	-0.027	0.352	-0.061	0.397	0.149	0.018
0.30	0.20	6.16	-20	30	0.6 (2.0)	6.1 (127)	0.373	-0.026	0.404	-0.052	0.370	0.149	-0.027
0.30	0.20	8.35	-20	30	0.6 (2.0)	6.1 (127)	0.170	-0.035	0.319		0.210	0.097	-0.021
0.30	5.10	1.54	-20	30	0.6 (2.0)	6.1 (127)	0.122	-0.048	-0.104		0.055	0.002	

TABLE 6. — Continued

M_∞	β, deg	α, deg	$\delta_{a,L}$, deg	δ_f, deg	$Re \times 10^{-6}$, per m (per ft)	q_∞, kPa (lb/ft²)	$n = 0.15$		$n = 0.80$		c_{m_W}	c_{D_W}	c_{R_W}
							c_n	c_m	c_n	c_m			
0.30	5.10	3.94	-20	30	0.6 (2.0)	6.1 (127)	0.241	-0.030	0.066	-0.070	0.180	0.054	0.008
0.30	5.10	6.24	-20	30	0.6 (2.0)	6.1 (127)	0.247	-0.022	0.192	-0.060	0.222	0.083	0.007
0.30	5.10	8.45	-20	30	0.6 (2.0)	6.1 (127)	0.007	-0.014	-0.159	-0.047	0.053	0.035	-0.041
0.30	9.60	1.59	-20	30	0.6 (2.0)	6.1 (127)	-0.050	-0.043	-0.466	0.062	-0.175	-0.108	0.024
0.30	9.60	3.99	-20	30	0.6 (2.0)	6.1 (128)	0.080	-0.033	-0.221	-0.056	-0.008	-0.030	-0.004
0.30	9.50	6.34	-20	30	0.6 (2.0)	6.1 (127)	0.049	-0.014	-0.004	-0.066	0.033	0.008	-0.022
0.30	9.50	8.58	-20	30	0.6 (2.0)	6.1 (128)	-0.175	-0.025	0.037	-0.034	-0.111	-0.025	-0.041
0.30	12.30	1.54	-20	30	0.6 (2.0)	6.0 (125)	-0.287	-0.056	-0.455	0.059	-0.329	-0.146	-0.049
0.30	12.20	3.98	-20	30	0.6 (2.0)	6.0 (125)	-0.044	-0.024	-0.450	0.007	-0.166	-0.104	0.018
0.30	12.20	6.36	-20	30	0.6 (2.0)	6.0 (125)	-0.164	-0.022	-0.147	-0.068	-0.153	-0.059	-0.037
0.30	12.20	8.55	-20	30	0.6 (2.0)	5.9 (125)	-0.251	-0.042	-0.043	-0.053	-0.179	-0.051	-0.049
0.70	-5.00	-0.71	0	0	1.0 (3.3)	23.6 (493)	0.701	-0.042	0.742	-0.058	0.691	0.277	0.056
0.70	-4.99	3.94	0	0	1.0 (3.3)	23.6 (493)	0.921	-0.120	0.401	-0.067	0.732	0.240	0.085
0.70	-4.95	7.94	0	0	1.0 (3.3)	23.6 (493)	0.778	-0.075	0.351	-0.053	0.622	0.205	0.091
0.70	0	-0.10	0	0	1.0 (3.3)	23.6 (493)	0.417	-0.054	0.347	-0.093	0.382	0.144	0
0.70	0	3.91	0	0	1.0 (3.3)	23.6 (493)	0.671	-0.021	0.614	-0.049	0.632	0.244	0.079
0.70	0	7.90	0	0	1.0 (3.3)	23.7 (494)	0.183	-0.042	0.430	-0.039	0.253	0.123	-0.040
0.70	5.00	-0.09	0	0	1.0 (3.3)	23.7 (494)	0.145	-0.056	-0.131	-0.068	0.063	0.001	-0.017
0.70	4.99	3.90	0	0	1.0 (3.3)	23.7 (494)	0.440	-0.038	0.316	-0.089	0.388	0.141	0.022
0.70	4.95	7.98	0	0	1.0 (3.3)	23.7 (494)	0.010	-0.011	0.254	-0.060	0.084	0.056	-0.052
0.70	-5.00	-2.10	0	0	1.7 (5.7)	40.7 (849)	0.520	-0.060	0.636	-0.085	0.538	0.223	-0.004
0.70	-5.00	-0.06	0	0	1.7 (5.7)	40.7 (849)	0.693	-0.040	0.774	-0.055	0.695	0.282	0.053
0.70	-5.00	1.95	0	0	1.7 (5.7)	40.7 (849)	0.828	-0.056	0.566	-0.064	0.721	0.260	0.093
0.70	0	-2.11	0	0	1.7 (5.7)	40.7 (850)	0.214	0.060	0.129	-0.102	0.181	0.063	0.049
0.70	0	-0.09	0	0	1.7 (5.7)	40.7 (850)	0.383	-0.050	0.327	-0.094	0.354	0.134	-0.004
0.70	0	1.91	0	0	1.7 (5.7)	40.7 (850)	0.566	-0.037	0.491	-0.081	0.525	0.200	0.041
0.70	0	3.88	0	0	1.7 (5.7)	40.7 (850)	0.686	-0.029	0.627	-0.057	0.646	0.249	0.073
0.70	5.00	-2.12	0	0	1.7 (5.7)	40.7 (850)	-0.026	-0.050	-0.193	-0.019	-0.070	-0.041	-0.033
0.70	5.00	-0.09	0	0	1.7 (5.7)	40.7 (850)	0.122	-0.054	0.076	-0.040	0.029	-0.016	-0.006
0.70	5.00	1.94	0	0	1.7 (5.7)	40.7 (850)	0.287	-0.050	0.267	-0.093	0.213	0.064	-0.005
0.70	4.99	3.91	0	0	1.7 (5.7)	40.7 (850)	0.424	-0.042	0.715	-0.084	0.362	0.128	0.021
0.78	-5.00	-0.09	0	0	1.0 (3.3)	25.6 (535)	0.771	-0.047	0.473	-0.065	0.729	0.282	0.070
0.78	-4.99	3.92	0	0	1.0 (3.3)	25.6 (535)	0.730	-0.042	0.364	-0.076	0.628	0.224	0.083
0.78	-4.95	7.94	0	0	1.0 (3.3)	25.6 (535)	0.723	-0.094	0.399	-0.058	0.590	0.199	0.060
0.78	0	-0.09	0	0	1.0 (3.3)	25.6 (535)	0.441	-0.051	0.364	-0.098	0.414	0.159	0.001
0.78	0	3.91	0	0	1.0 (3.3)	25.6 (535)	0.446	-0.037	0.543	-0.051	0.461	0.191	0.015
0.78	0	7.89	0	0	1.0 (3.3)	25.6 (535)	0.134	-0.039	0.439	-0.045	0.222	0.117	-0.054
0.78	5.00	-0.10	0	0	1.0 (3.3)	25.6 (535)	0.159	-0.058	-0.118	-0.072	0.076	0.006	-0.018
0.78	4.99	3.92	0	0	1.0 (3.3)	25.6 (535)	0.407	-0.052	0.342	-0.093	0.374	0.142	-0.001
0.78	4.95	7.90	0	0	1.0 (3.3)	25.6 (535)	-0.036	-0.002	0.210	-0.063	0.036	0.036	-0.054
0.78	-5.00	-2.10	0	0	1.6 (5.3)	40.7 (849)	0.529	-0.058	0.701	-0.080	0.564	0.239	-0.004
0.78	-5.00	-0.04	0	0	1.6 (5.3)	40.7 (849)	0.751	-0.045	0.857	-0.061	0.759	0.310	0.054
0.78	-5.00	1.96	0	0	1.6 (5.3)	40.7 (849)	0.791	-0.145	0.477	-0.073	0.669	0.235	0.023
0.78	-4.99	3.95	0	0	1.6 (5.3)	40.7 (849)	0.867	-0.096	0.392	-0.062	0.694	0.229	0.091
0.78	0	-2.15	0	0	1.6 (5.3)	40.7 (850)	0.226	-0.096	0.141	-0.106	0.192	0.068	-0.065

TABLE 6. — Concluded

M_∞	β, deg	α, deg	$\delta_{a,L}$, deg	δ_ℓ, deg	$Re \times 10^{-6}$, per m (per ft)	q_∞, kPa (lb/ft²)	n = 0.15		n = 0.80		c_{N_W}	c_{B_W}	c_{T_W}
							c_n	c_m	c_n	c_m			
0.78	0	-0.09	0	0	1.6 (5.3)	40.7 (851)	0.404	-0.048	0.369	-0.098	0.380	0.147	-0.003
0.78	0	1.92	0	0	1.6 (5.3)	40.7 (850)	0.585	-0.033	0.568	-0.074	0.561	0.220	0.044
0.78	0	3.89	0	0	1.6 (5.3)	40.7 (851)	0.645	-0.033	0.602	-0.039	0.610	0.237	0.068
0.78	5.00	-2.10	0	0	1.6 (5.3)	40.7 (850)	-0.019	-0.051	-0.147	-0.026	-0.058	-0.035	-0.038
0.78	5.00	-0.08	0	0	1.6 (5.3)	40.7 (849)	0.134	-0.054	-0.155	-0.057	0.048	-0.006	-0.013
0.78	5.00	1.91	0	0	1.6 (5.3)	40.7 (850)	0.315	-0.049	0.115	-0.098	0.243	0.077	-0.002
0.78	4.99	3.90	0	0	1.6 (5.3)	40.7 (849)	0.455	-0.057	0.320	-0.087	0.399	0.145	0.012
0.90	-5.00	-0.11	0	0	1.0 (3.3)	28.1 (587)	0.604	-0.054	0.586	-0.074	0.579	0.227	0.031
0.90	-4.99	3.94	0	0	1.0 (3.3)	28.1 (587)	0.464	-0.066	0.682	-0.111	0.515	0.224	-0.036
0.90	-4.95	7.94	0	0	1.0 (3.3)	28.1 (587)	0.308	-0.050	0.750	-0.134	0.433	0.212	-0.079
0.90	0	-0.07	0	0	1.0 (3.3)	28.1 (586)	0.379	-0.042	0.429	-0.120	0.382	0.156	-0.019
0.90	0	3.92	0	0	1.0 (3.3)	28.1 (586)	0.320	-0.065	0.518	-0.083	0.370	0.165	-0.046
0.90	0	7.90	0	0	1.0 (3.3)	28.0 (585)	0.093	-0.036	0.474	-0.075	0.207	0.117	-0.076
0.90	5.00	-0.13	0	0	1.0 (3.3)	28.1 (587)	0.183	-0.060	-0.068	-0.093	0.108	0.021	-0.026
0.90	4.99	3.91	0	0	1.0 (3.3)	28.1 (587)	0.095	-0.021	0.235	-0.106	0.135	0.066	-0.053
0.90	4.95	7.91	0	0	1.0 (3.3)	28.1 (587)	-0.108	0.013	0.211	-0.087	-0.014	0.023	-0.069
0.90	-5.00	-2.12	0	0	1.5 (4.8)	40.7 (850)	0.425	-0.072	0.575	-0.105	0.457	0.194	-0.038
0.90	-5.00	-0.07	0	0	1.5 (4.8)	40.7 (850)	0.444	-0.059	0.699	-0.105	0.507	0.224	-0.036
0.90	-5.00	1.97	0	0	1.5 (4.8)	40.7 (850)	0.501	-0.046	0.762	-0.103	0.564	0.247	-0.017
0.90	-4.99	3.93	0	0	1.5 (4.8)	40.7 (850)	0.623	-0.089	0.387	-0.064	0.531	0.187	0.034
0.90	0	-2.08	0	0	1.5 (4.8)	40.7 (850)	0.201	-0.062	0.148	-0.123	0.178	0.065	-0.053
0.90	0	-0.08	0	0	1.5 (4.8)	40.7 (850)	0.352	-0.047	0.378	-0.114	0.349	0.140	-0.023
0.90	0	1.96	0	0	1.5 (4.8)	40.7 (850)	0.334	-0.042	0.489	-0.097	0.370	0.161	-0.028
0.95	-5.00	3.91	0	0	1.0 (3.4)	29.6 (618)	0.306	-0.059	0.489	-0.067	0.352	0.156	-0.037
0.95	-5.00	-0.11	0	0	1.0 (3.4)	29.6 (619)	0.342	-0.047	0.225	-0.058	0.295	0.105	-0.010
0.95	-5.00	3.96	0	0	1.0 (3.4)	29.6 (618)	0.688	-0.131	0.438	-0.096	0.589	0.209	0.003
0.95	-4.99	7.95	0	0	1.0 (3.4)	29.6 (619)	0.837	-0.150	0.636	-0.139	0.748	0.277	-0.008
0.95	0	-0.32	0	0	1.0 (3.4)	29.6 (619)	0.135	-0.031	0.257	-0.116	0.168	0.078	-0.056
0.95	0	3.91	0	0	1.0 (3.4)	29.6 (619)	0.213	-0.006	0.358	-0.082	0.250	0.112	-0.015
0.95	0	7.91	0	0	1.0 (3.4)	29.6 (618)	0.215	-0.040	0.629	-0.134	0.334	0.171	-0.084
0.95	5.00	-0.11	0	0	1.0 (3.4)	29.6 (619)	0.080	-0.053	-0.232	-0.033	-0.011	-0.032	-0.009
0.95	5.00	3.96	0	0	1.0 (3.4)	29.6 (619)	0.119	-0.057	0.192	-0.110	0.137	0.061	-0.070
0.95	-5.00	-0.41	0	0	1.2 (3.8)	33.8 (706)	-0.143	-0.048	0.140	-0.073	-0.059	0.002	-0.040
0.95	-5.00	1.85	0	0	1.2 (3.8)	33.8 (706)	0.243	-0.006	0.285	-0.067	0.248	0.102	0.005
0.95	-5.00	3.96	0	0	1.2 (3.8)	33.9 (707)	0.516	-0.105	0.323	-0.066	0.440	0.155	0
0.95	-4.99	5.98	0	0	1.2 (3.8)	33.8 (706)	0.596	-0.140	0.433	-0.096	0.526	0.193	-0.027
0.95	-4.97	7.96	0	0	1.2 (3.8)	33.9 (707)	0.665	-0.141	0.508	-0.110	0.596	0.220	-0.023
0.95	0	-0.26	0	0	1.2 (3.8)	33.9 (707)	0.151	-0.027	0.247	-0.110	0.175	0.078	-0.045
0.95	0	1.83	0	0	1.2 (3.8)	33.9 (707)	0.219	-0.015	0.353	-0.086	0.253	0.112	-0.020
0.95	0	3.91	0	0	1.2 (3.8)	33.9 (707)	0.385	-0.044	0.189	-0.063	0.313	0.105	0.025
0.95	0	5.90	0	0	1.2 (3.8)	33.9 (708)	0.275	-0.026	0.457	-0.089	0.321	0.144	-0.025
0.95	5.00	-0.14	0	0	1.2 (3.8)	33.9 (707)	0.058	-0.054	-0.270	-0.012	-0.038	-0.044	-0.005
0.95	5.00	1.75	0	0	1.2 (3.8)	33.9 (707)	0.106	-0.038	0.050	-0.112	0.085	0.029	-0.046
0.95	4.99	3.94	0	0	1.2 (3.8)	33.9 (707)	0.023	-0.024	0.142	-0.094	0.058	0.034	-0.060
0.95	4.97	5.93	0	0	1.2 (3.8)	33.9 (707)	-0.137	0.039	0.154	-0.091	-0.051	0.005	-0.053
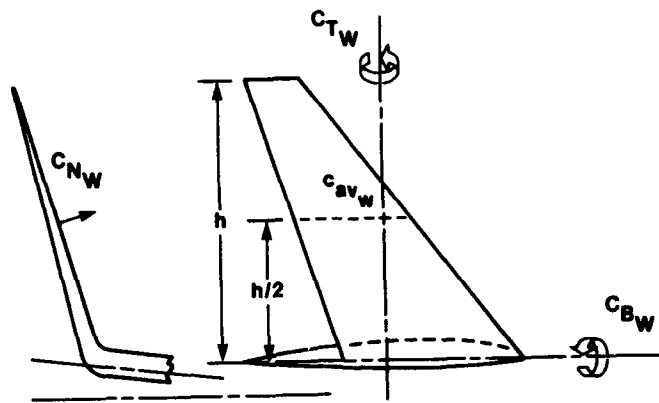
Figure 1. Winglet sign convention. Left winglet is shown with positive values of forces and moments.
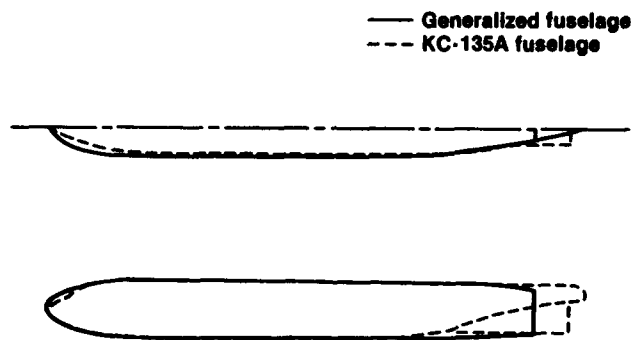
Figure 2. Comparison of generalized fuselage with actual KC-135A aircraft model fuselage.

Figure 3. Typical outboard wing airfoil section.
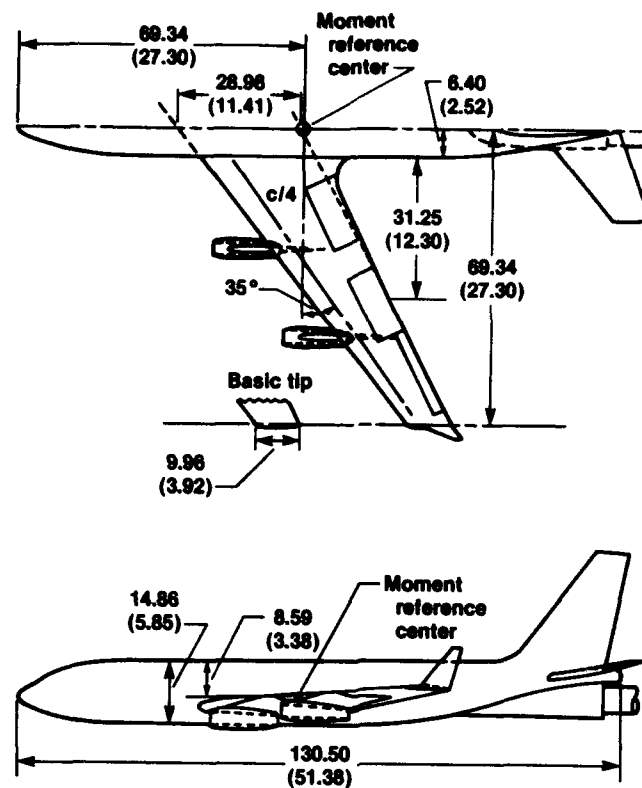
(a) General arrangement.
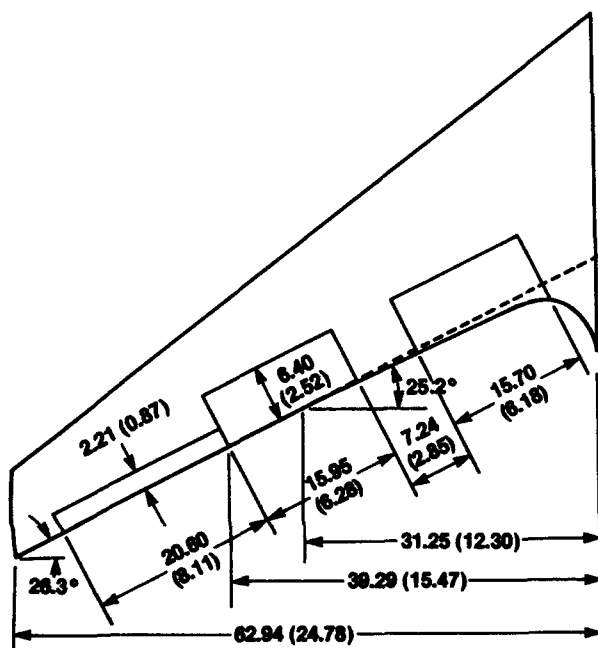
(b) Flap and aileron detail.
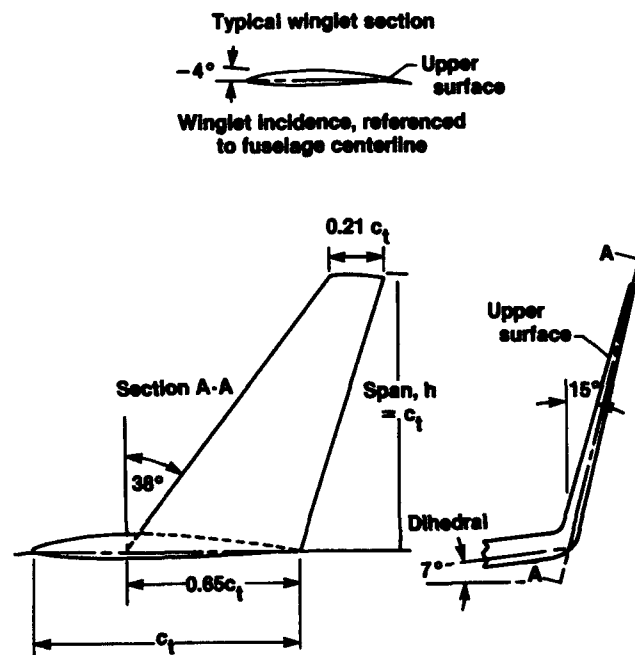
(c) Winglet details.

Figure 4. Drawings of a 0.035-scale, full span KC-135A low-speed aircraft model. Dimensions are in centimeters (inches).
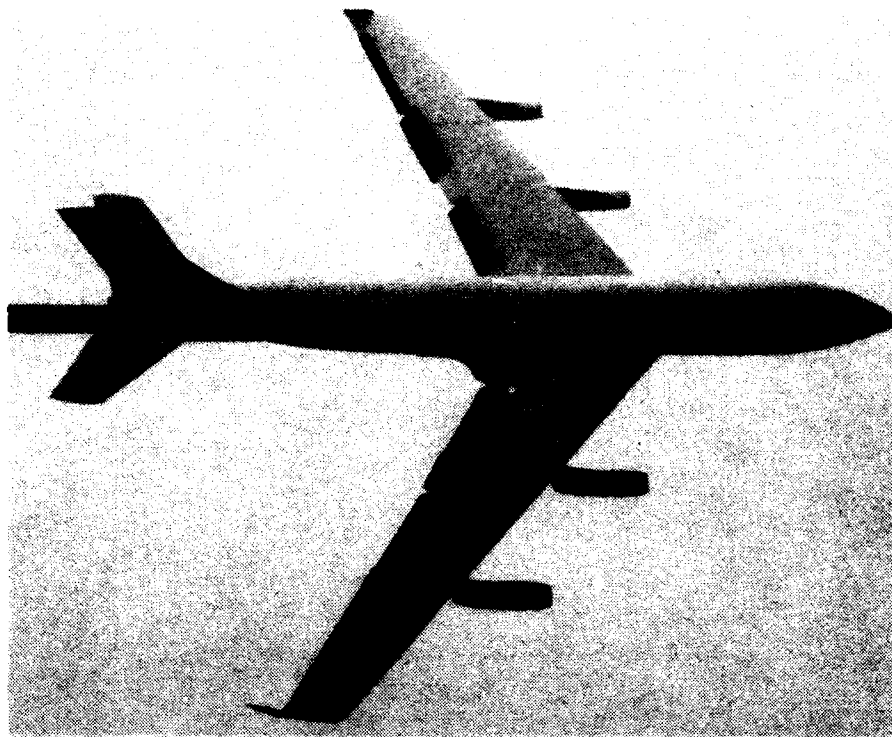
(a) General arrangement.
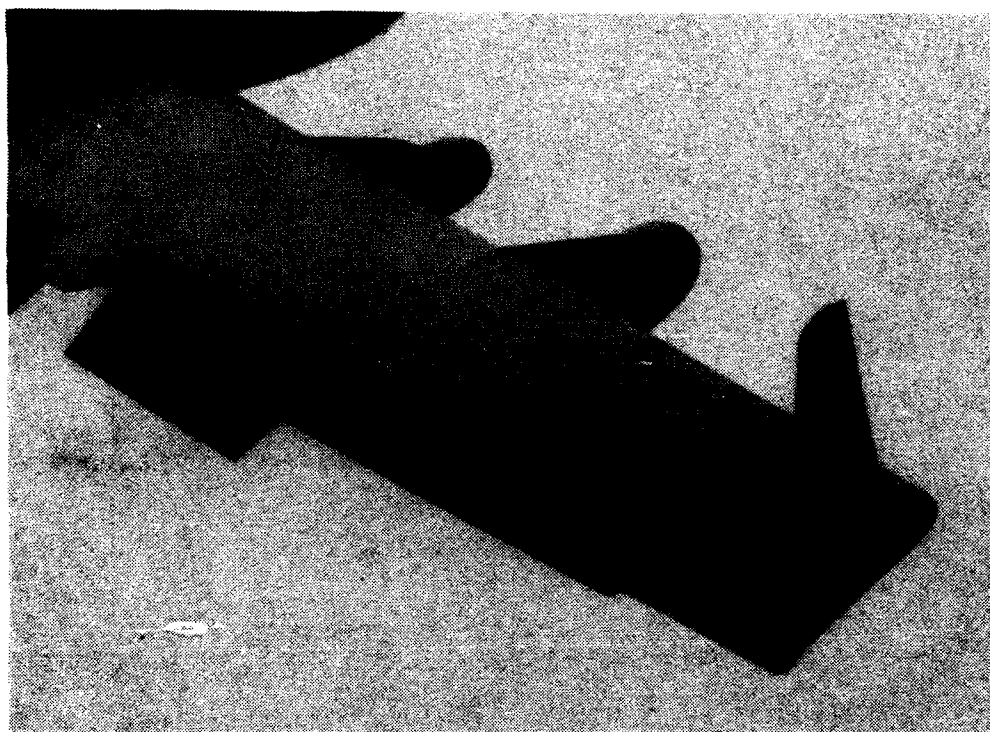
(b) Winglet, aileron, and flap.

Figure 5. KC-135A full span low-speed aircraft model with winglets.
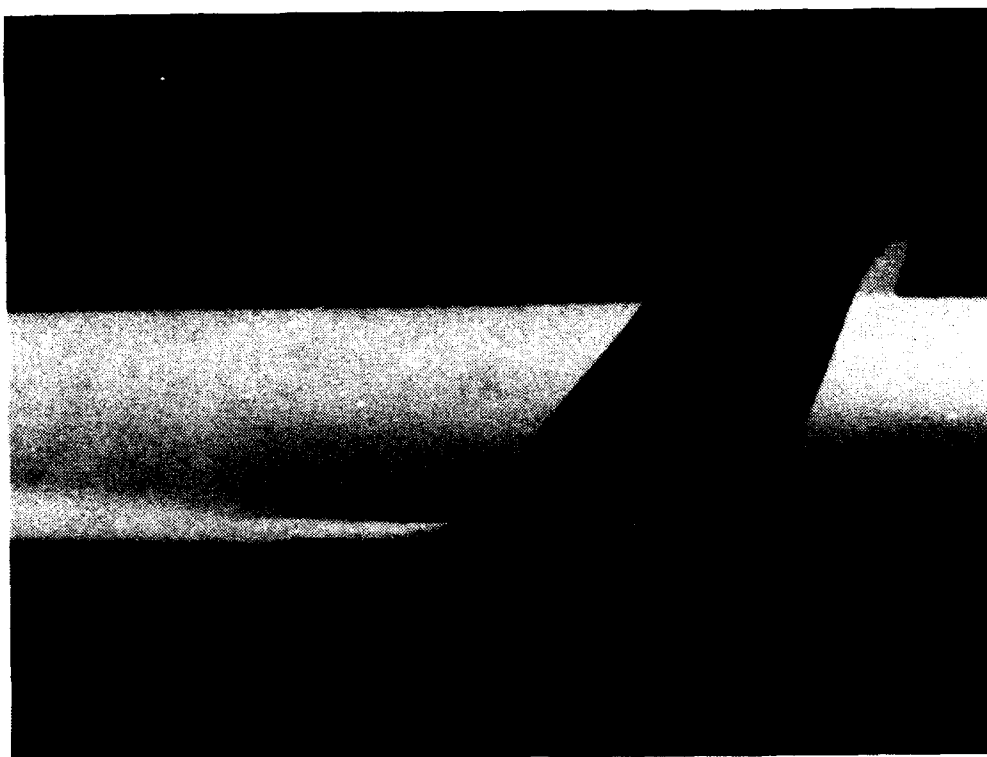
(c) Winglet.

Figure 5.   Concluded.

28.98
(11.41)

Moment reference center

70.41
(27.72)

37.55°

27.99
(11.02)

37.64
(14.82)

Trailing-edge break

48.44
(19.07)

69.34
(27.30)

9.96
(3.92)

7.29
(2.87) Radius

125.88
(49.56)

Moment reference center
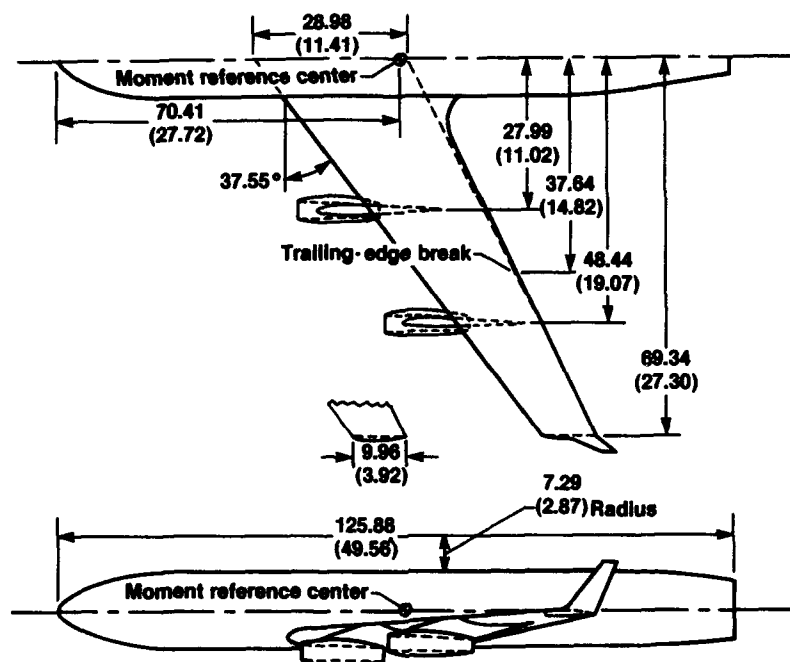
Figure 6.   General layout of high-speed model.
Dimensions are in centimeters (inches).
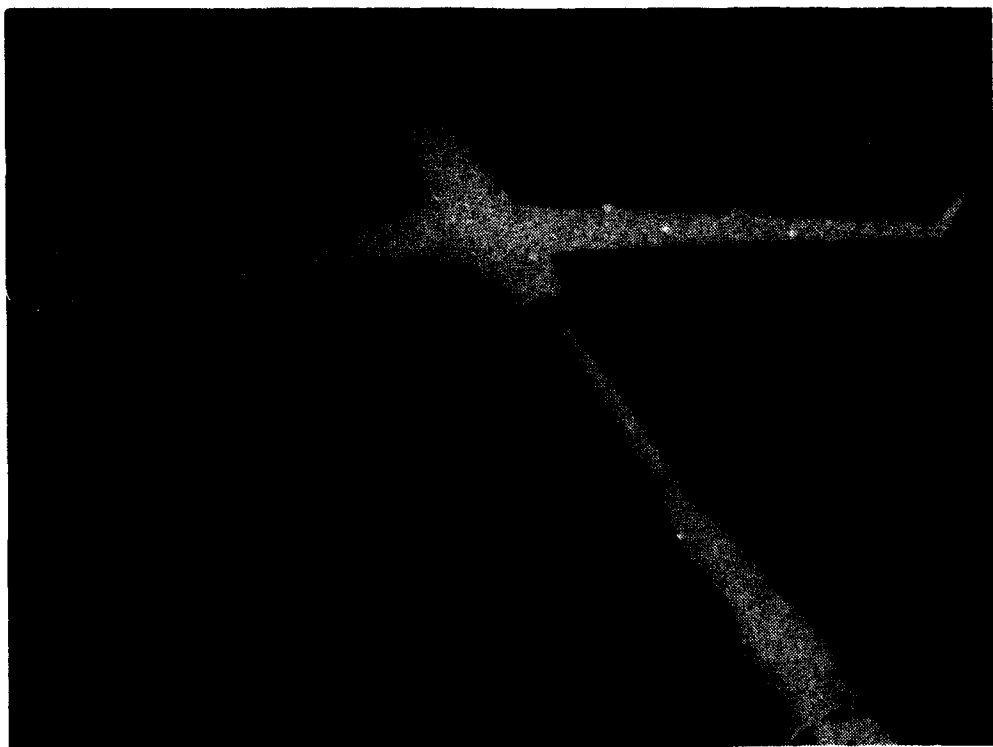
Figure 7. Wind-tunnel high-speed model.

WING ORIFICE LOCATIONS
(u, upper surface orifice; l, lower surface orifice)

x/c	η						
	0.128	0.256	0.385	0.641	0.821	0.921	0.979
0	u	...	...	u	u	u	u
0.020	u	u	u	u	u	u	u
0.025	...	l	l	l	l	l	...
0.050	u	u	u	u	u	...	u
0.075	l	l	l	l	l	l	l
0.100	u	u	u	u	u	u	l
0.150	u, l	u	u, l	u, l	u, l	u	u, l
0.250	u, l	u, l	u, l	u, l	u, l	u, l	u, l
0.350	u	u	u	...	u	u	u
0.400	l	l	l	l	l	l	l
0.450	u	u	u	u	u	u	u
0.550	u, l	u, l	u, l	u, l	u, l	u, l	u, l
0.650	u	u	u	u	u	u	u
0.750	u, l	u, l	u, l	u, l	u, l	u, l	u, l
0.850	u, l	u, l	u, l	u, l	u, l	u, l	u, l
0.950	l	l	l	l	l	l	l
0.980	...	u	u	u	u	u	...
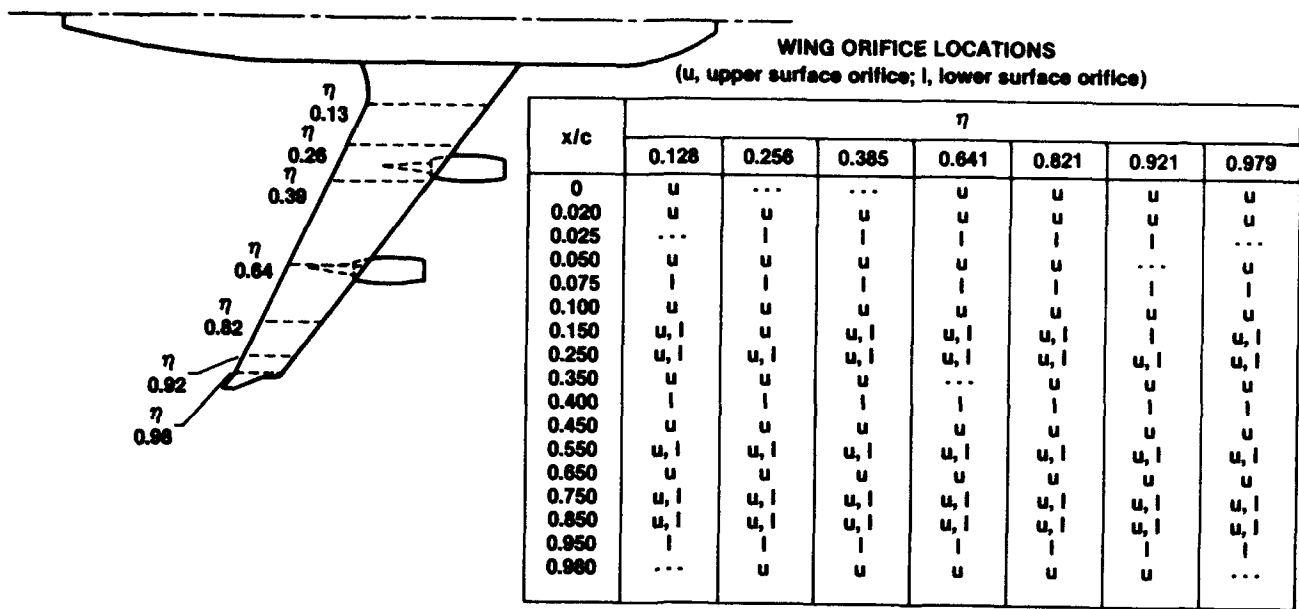
(a) Right wing, high-speed model only.

Winglet orifice locations
(u, upper surface orifice; l, lower surface orifice)

x/c	η	
	0.150	0.800
0.005	u	u
0.025	u	u
0.050	u	u
0.080	u	u
0.200	u	u
0.225	l	l
0.350	u	u
0.400	l	...
0.500	u	u
0.600	l	l
0.650	u	u
0.775	l	l
0.800	u	u
0.900	...	u, l
0.950	u, l	...
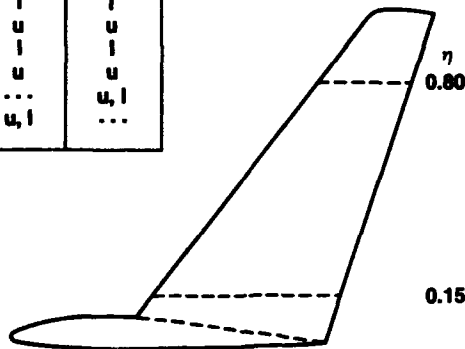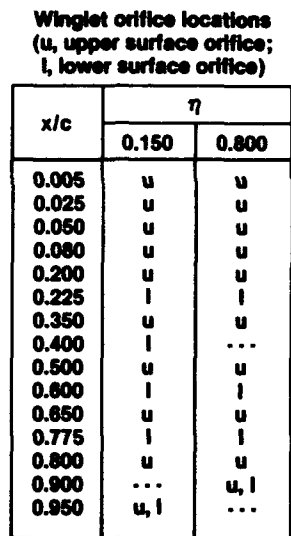
(b) Left winglet, both models.

Figure 8. Wing and winglet static-pressure orifice locations.
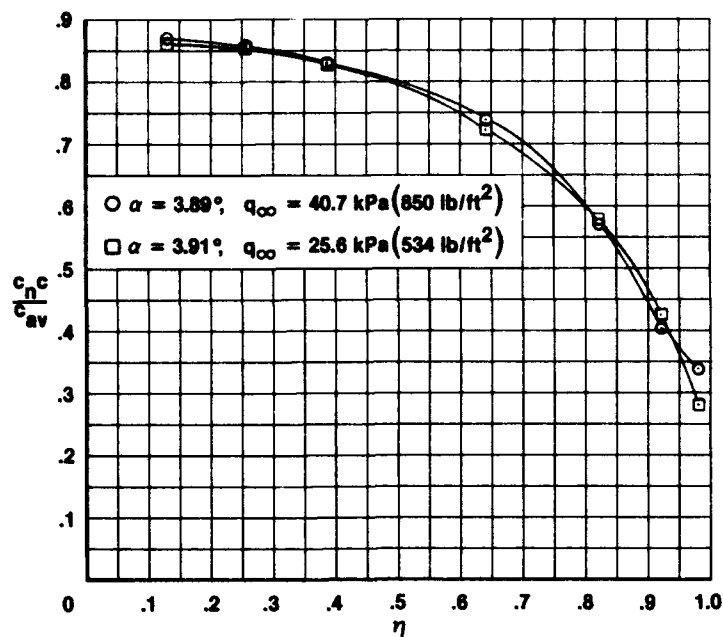
Figure 9. Comparison of full-span model spanwise loads at two dynamic pressures. $M_\infty = 0.78$.
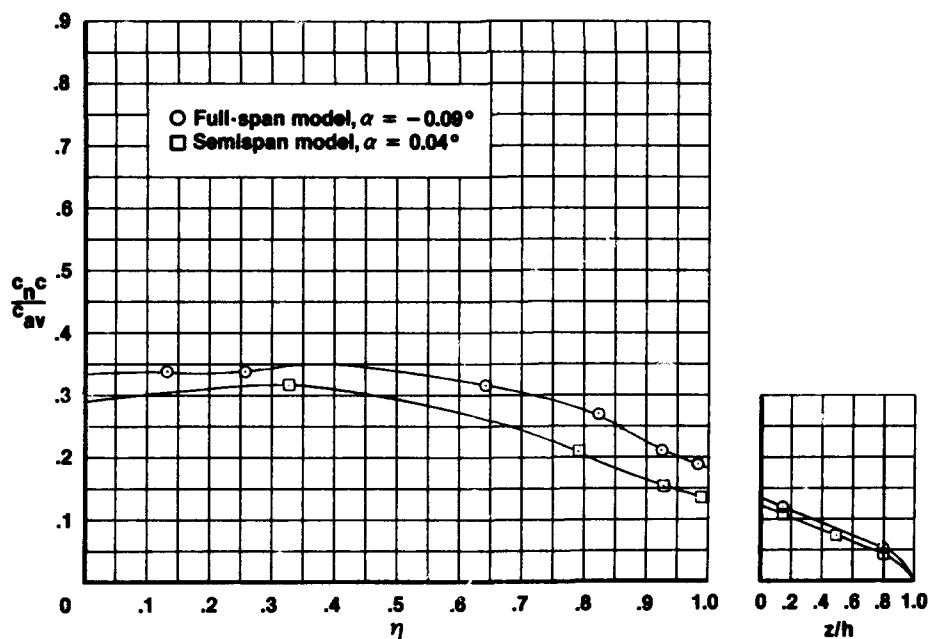
(a) Approximately 0° angle of attack.

Figure 10. Comparison of full-span model and semispan model wing and winglet spanwise load distributions. $M_\infty = 0.78$; $q_\infty = 40.7$ kPa (850 lb/ft²).
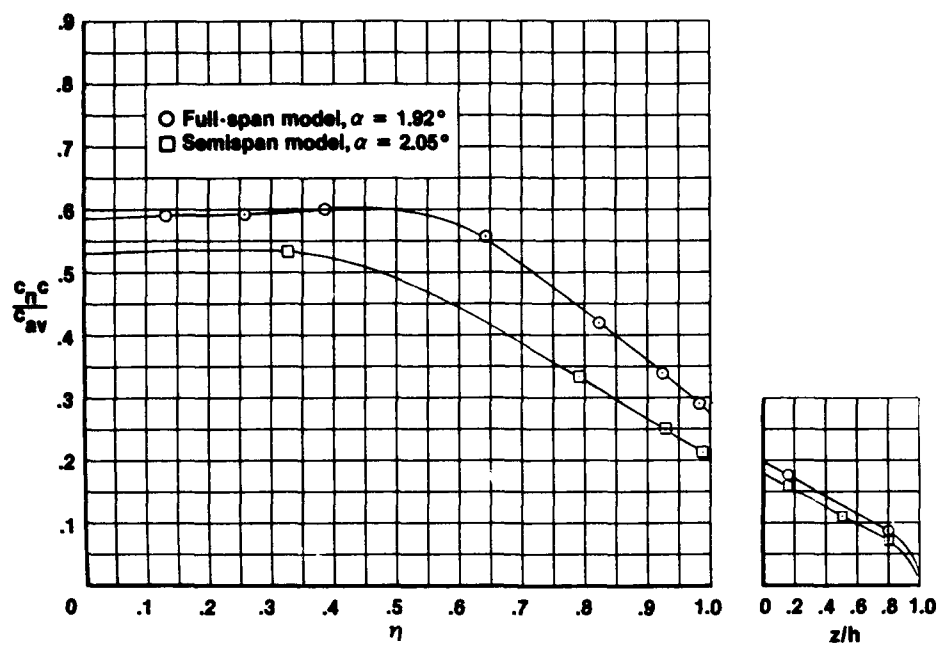
(b) Approximately 2.0° angle of attack.
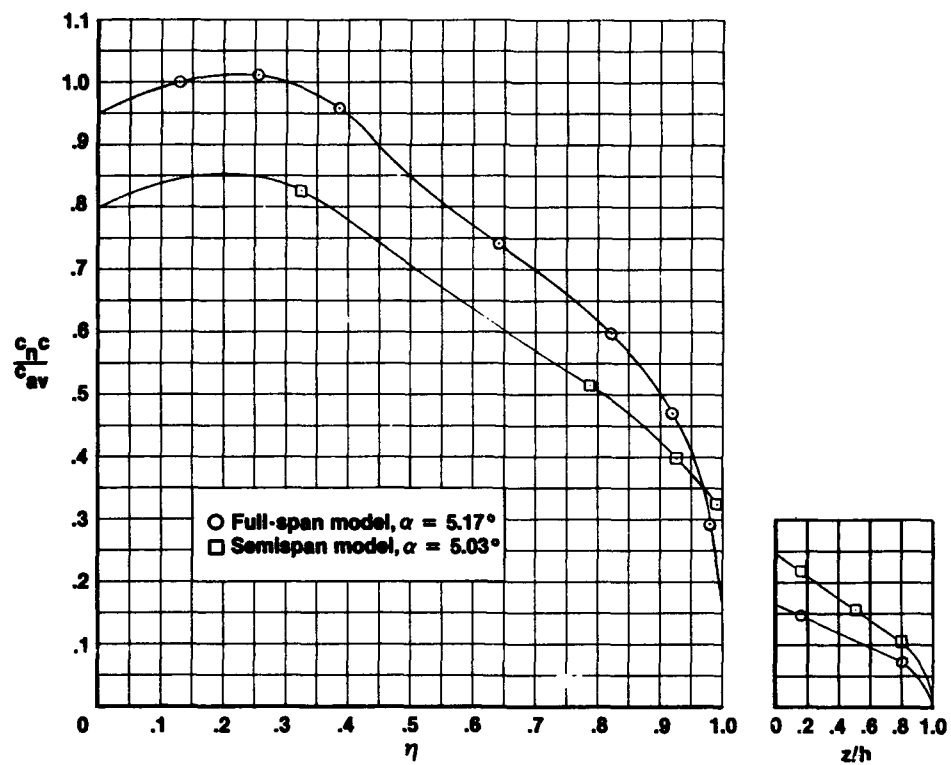
(c) Approximately 5.1° angle of attack.

Figure 10.   Concluded.
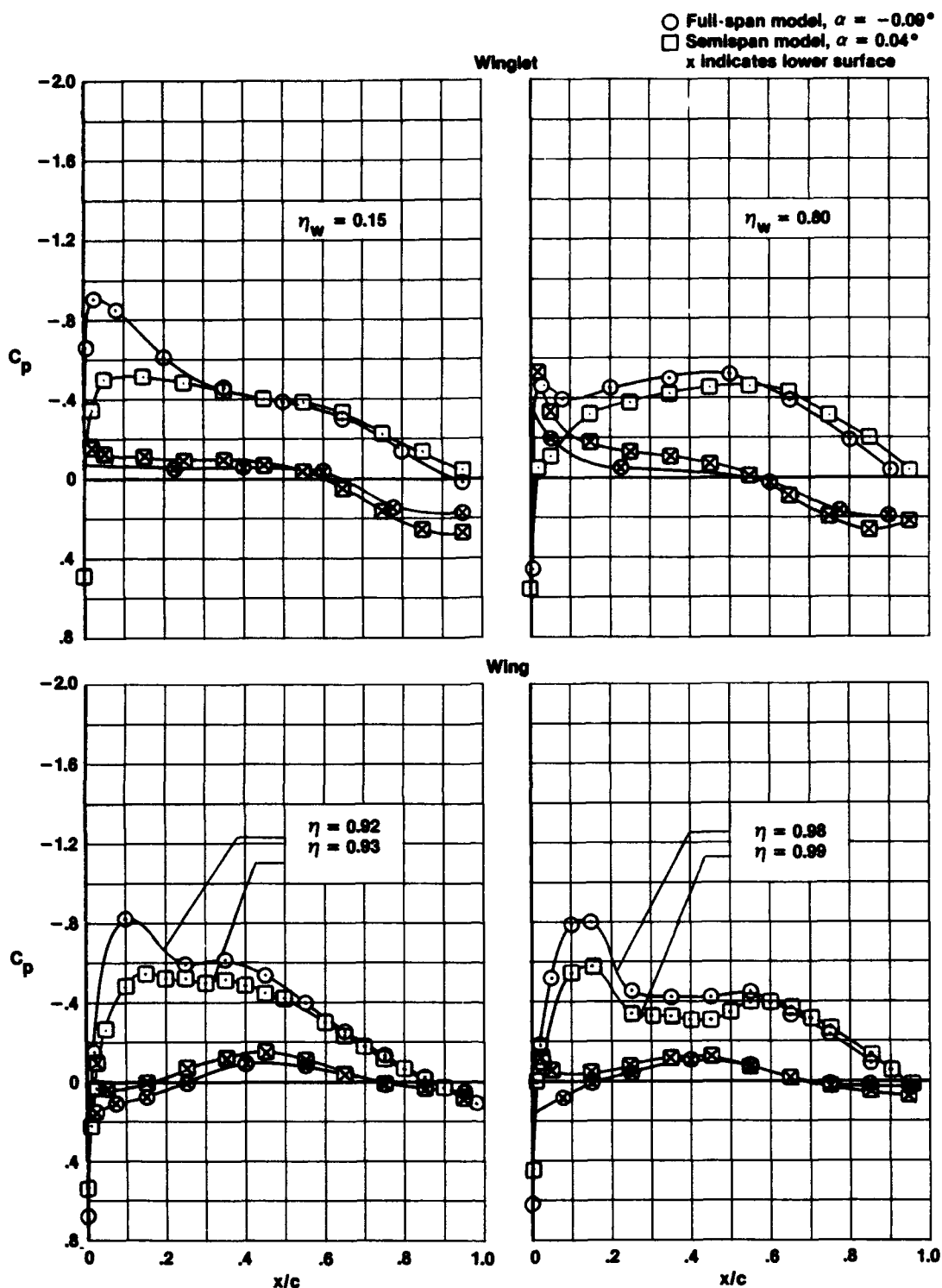
(a) Approximately 0° angle of attack.

Figure 11. Comparison of full-span model and semispan model wing and winglet chordwise pressure distributions. $M = 0.78$; $q = 40.7$ kPa (850 lb/ft^2).
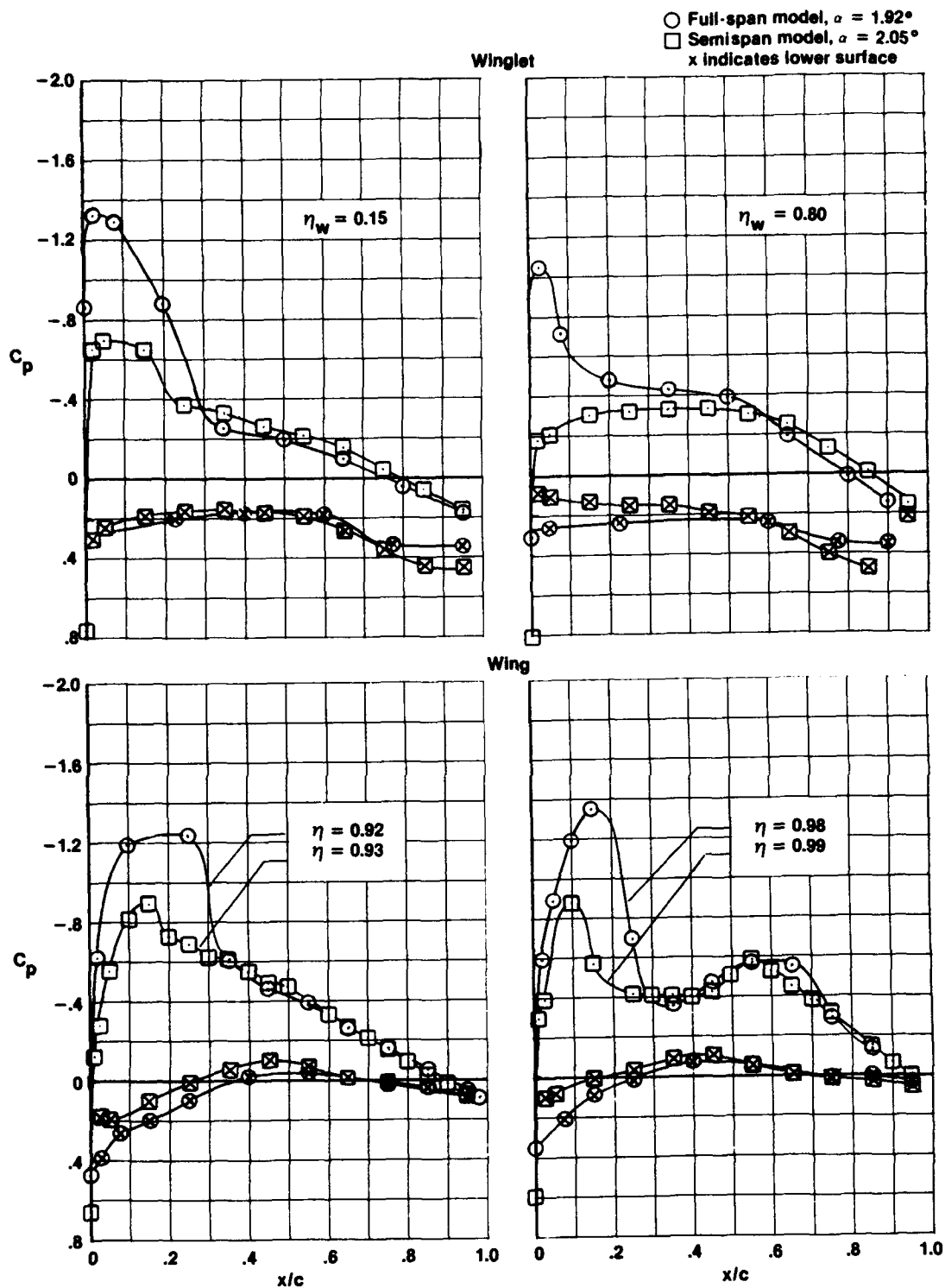
(b) Approximately 2.0° angle of attack.

Figure 11. Continued.
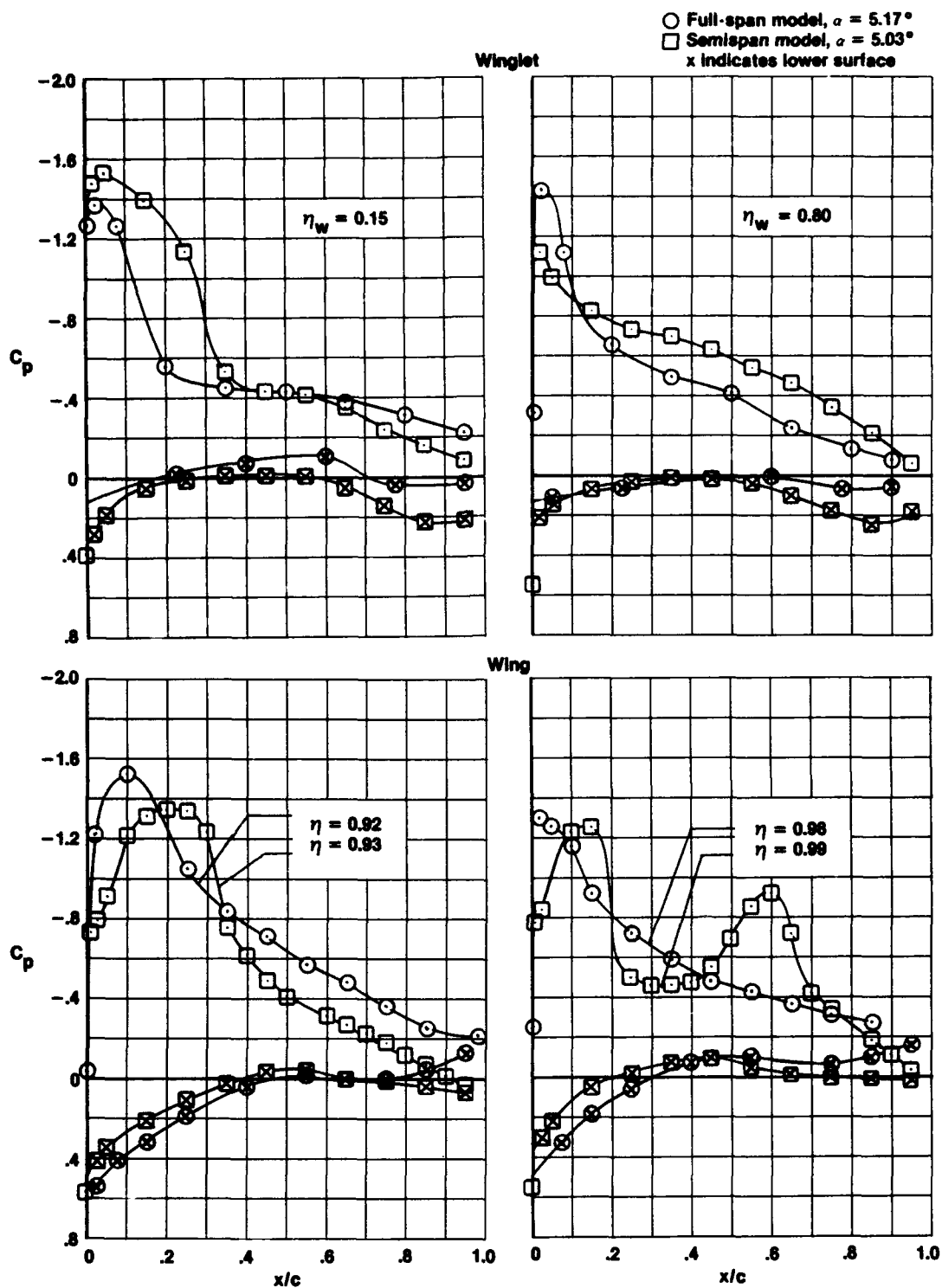
(c) Approximately 5.1° angle of attack.

Figure 11. Concluded.
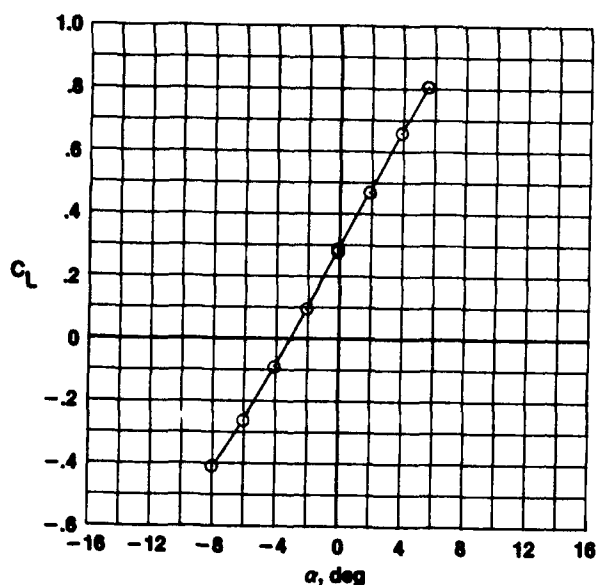
(a) $M_\infty = 0.70$; $q_\infty = 40.7$ kPa (850 lb/ft^2).
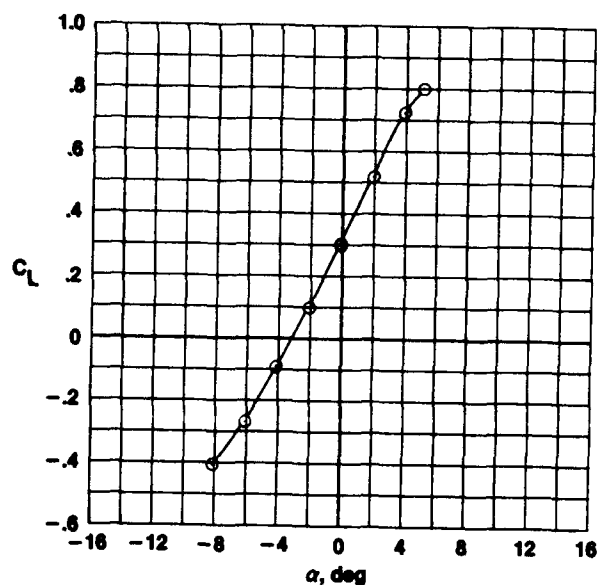
(b) $M_\infty = 0.78$; $q_\infty = 40.7$ kPa (850 lb/ft^2).
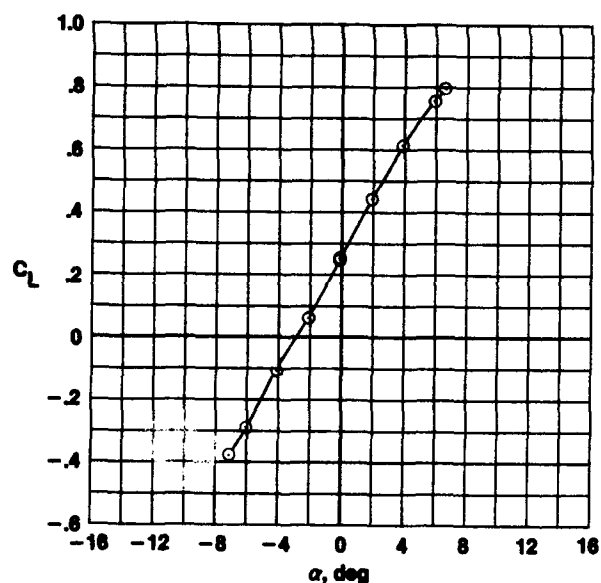
(c) $M_\infty = 0.90$; $q_\infty = 40.7$ kPa (850 lb/ft^2).
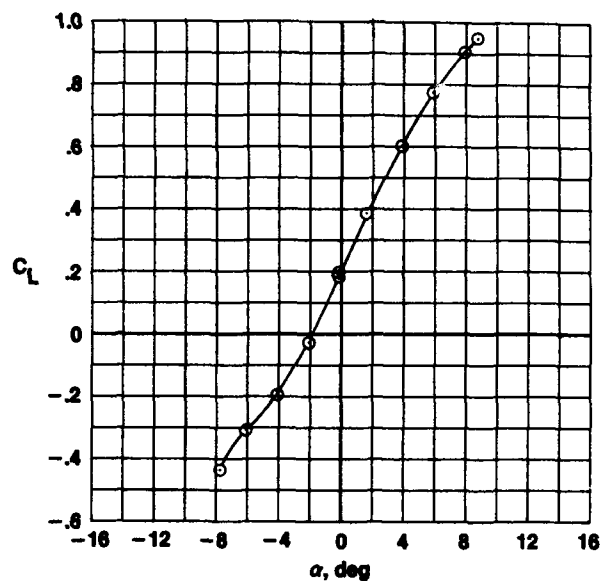
(d) $M_\infty = 0.95$; $q_\infty = 33.8$ kPa (707 lb/ft^2).

Figure 12. Variation of full-span high-speed model lift coefficient with angle of attack for several Mach numbers.
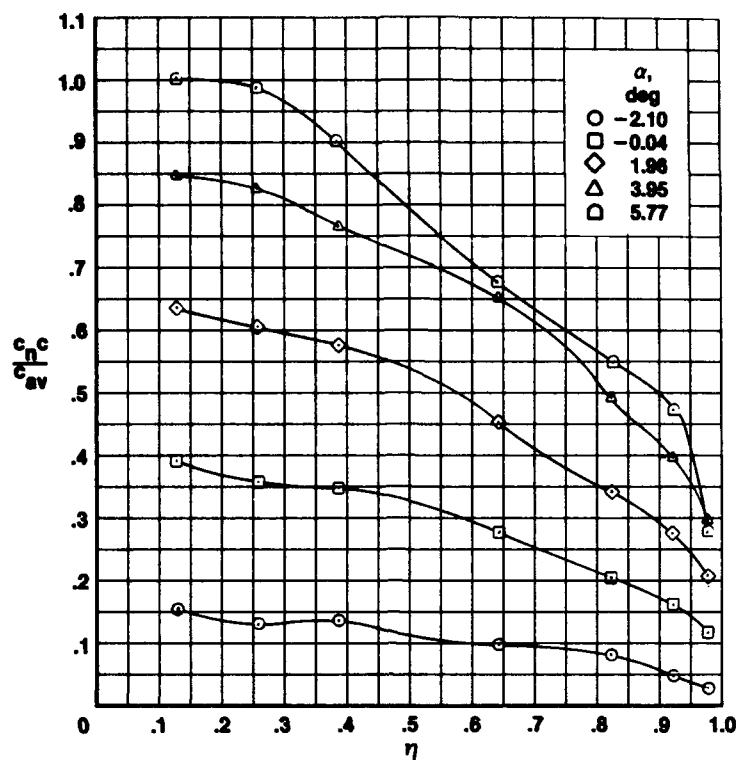
(a) β = -5°.

Figure 13. Variation of full-span model right wing panel span load distributions with winglets for several angles of attack at selected sideslip angles. $M_\infty = 0.78$; $q_\infty = 40.7$ kPa (850 lb/ft²).

(b) β = 0°.
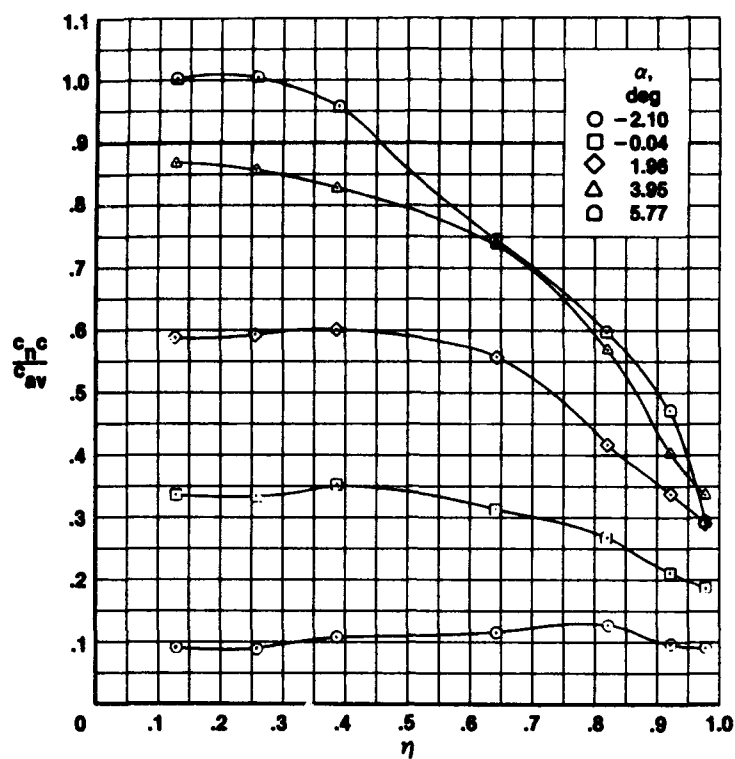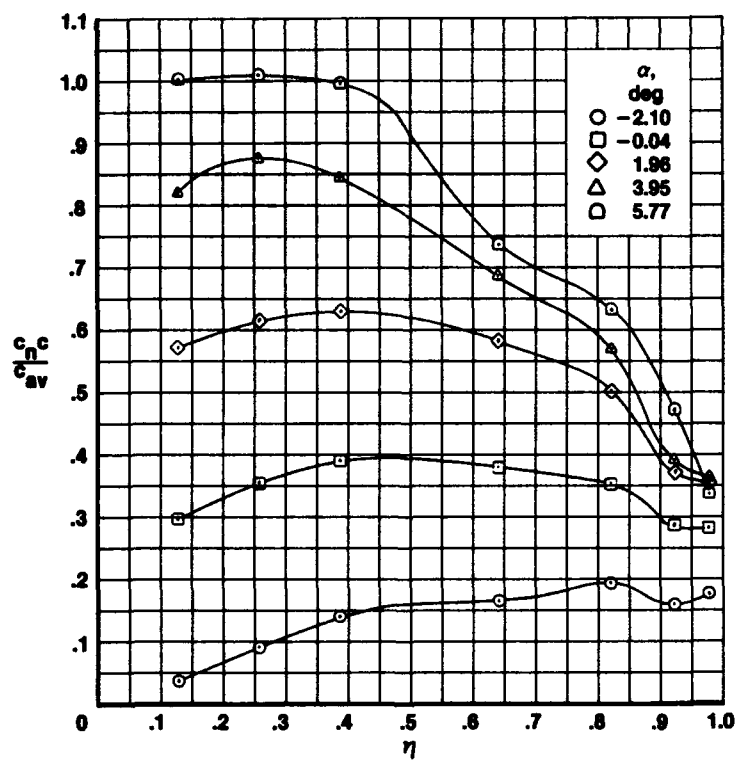
(c) β = 5°.

Figure 13. Concluded.
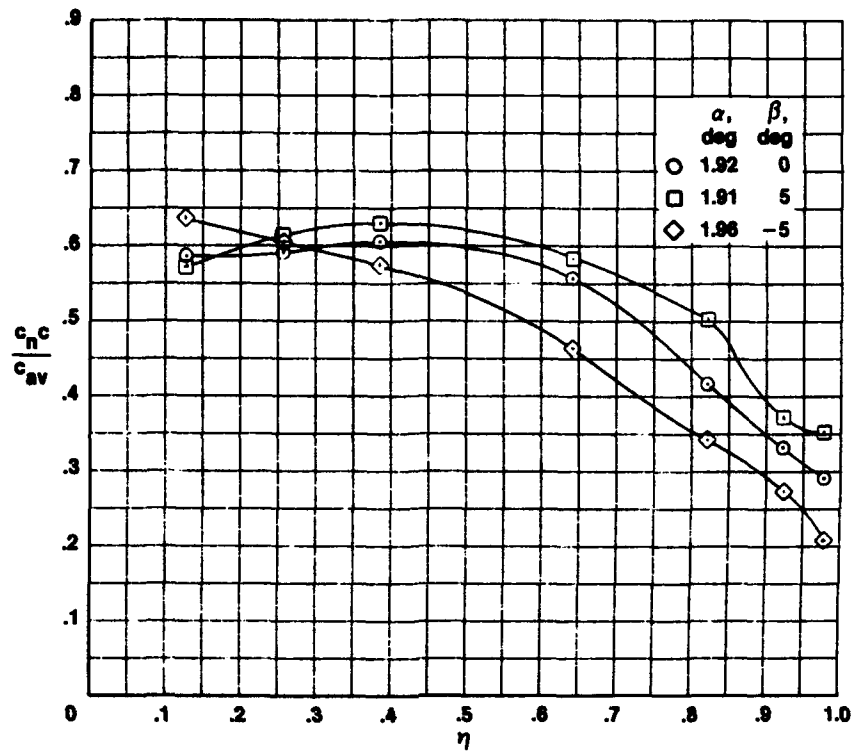
Figure 14. Variation of full-span model right wing panel load distributions with winglets for several angles of sideslip at a selected angle of attack. $M_\infty = 0.78$; $q_\infty = 40.7$ kPa (850 lb/ft^2).
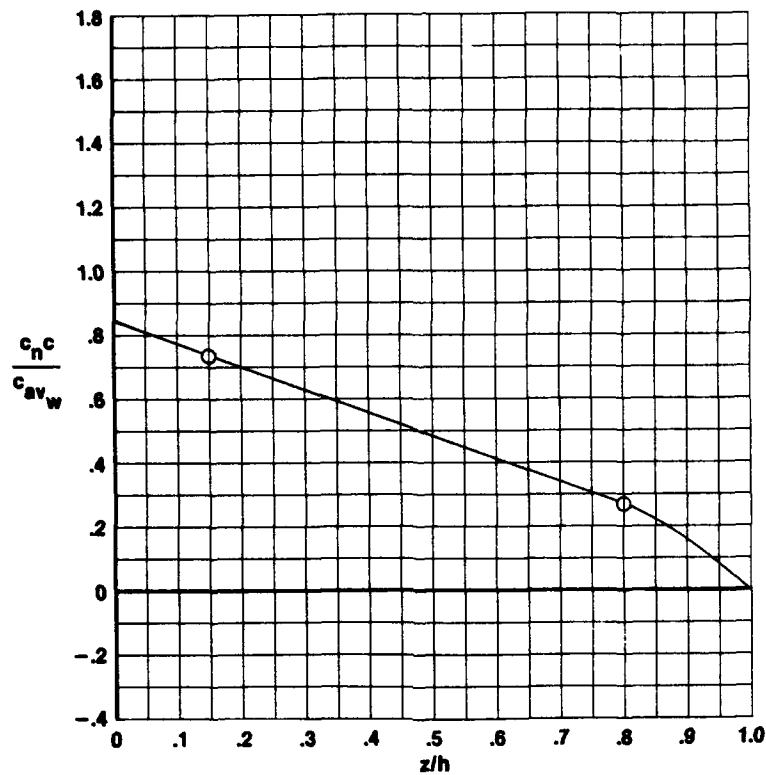
(a) $\alpha = 1.5°$; $\beta = 0.2°$.

Figure 15. Variation of left winglet span-
wise load distribution for several angles of
attack at a sideslip angle of 0.2° in a take-
off configuration. $M_\infty = 0.30$; $\delta_f = 30°$;
$\delta_{a,L} = 0°$; and $\delta_{a,R} = 0°$.

(b) α = 3.9°; β = 0.2°.
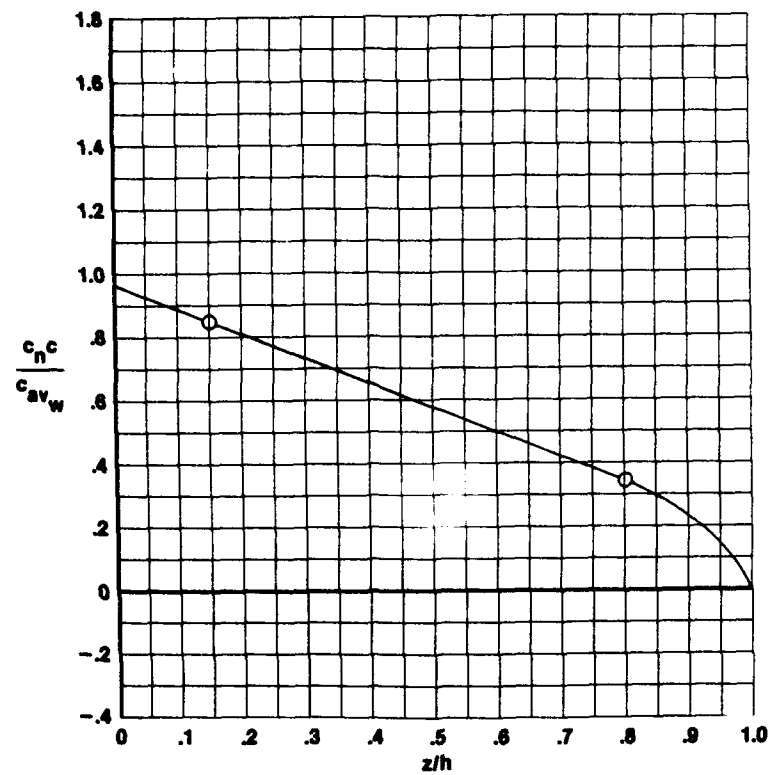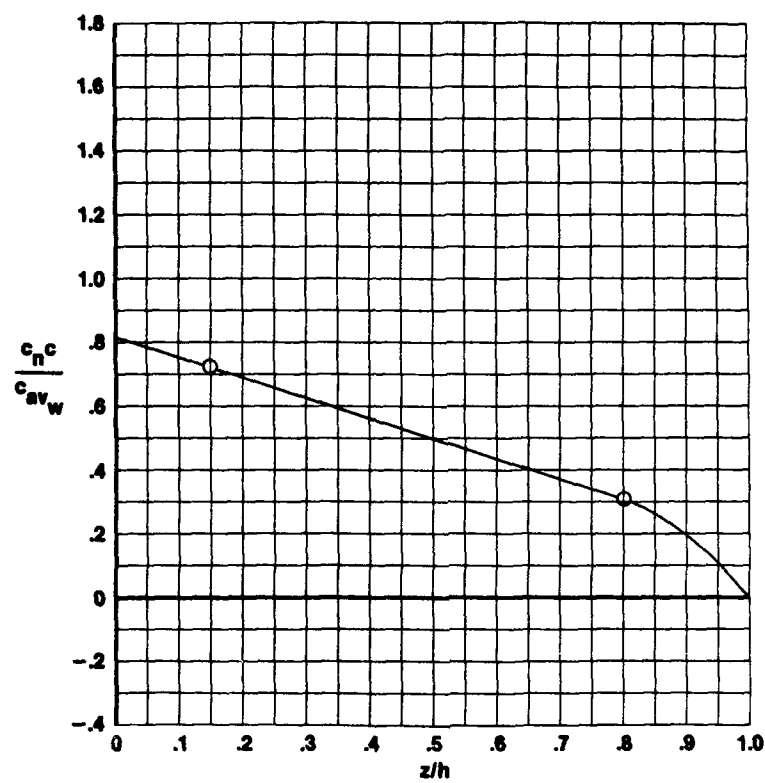
(c) α = 6.2°; β = 0.2°.

Figure 15. Continued.
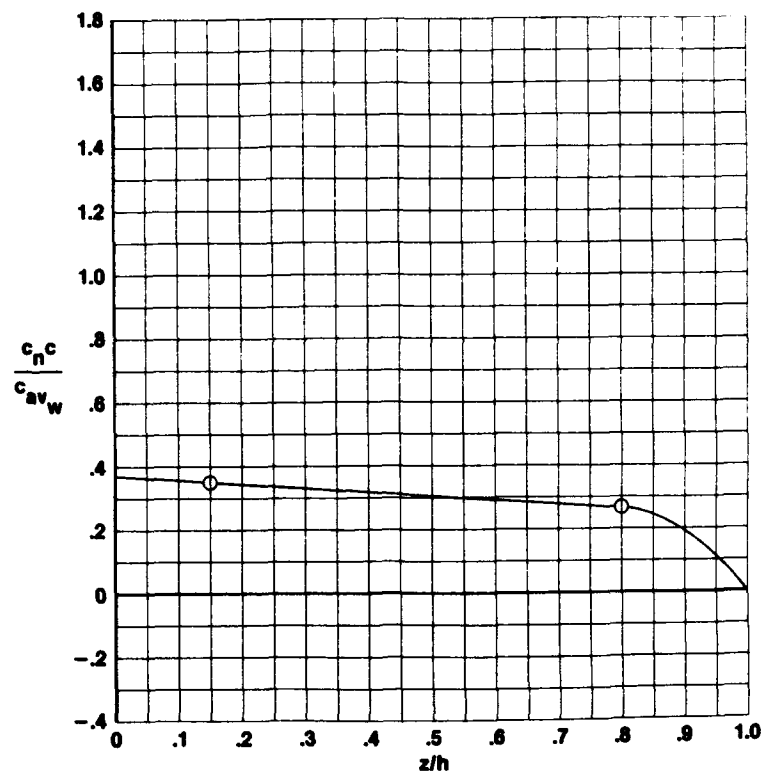
(d) α = 8.4°; β = 0.2°.

Figure 15. Concluded.
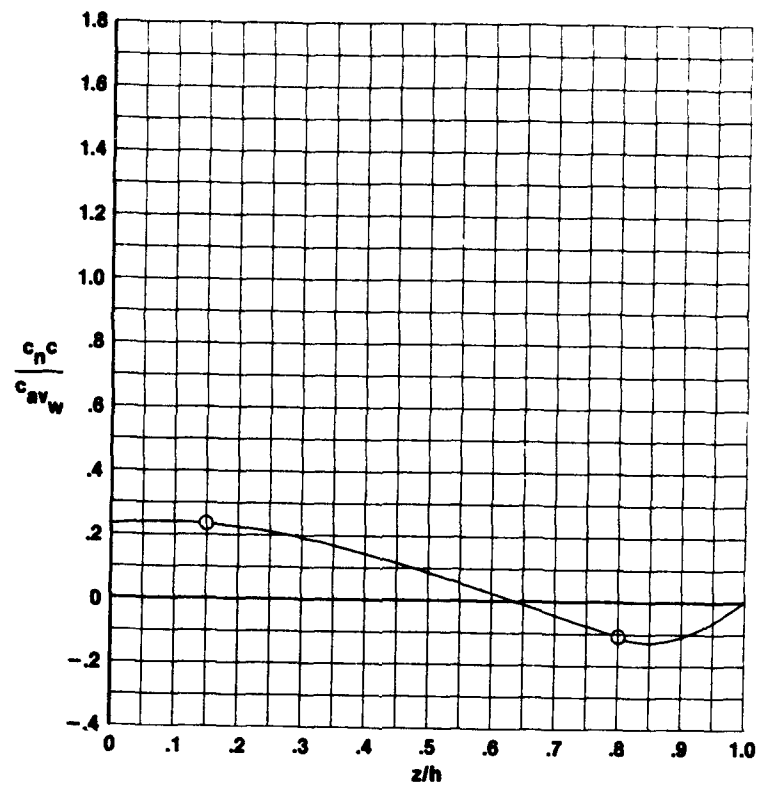
(a) $\alpha = 4.0°$; $\beta = 12.2°$.

Figure 16. Variation of left winglet span-wise load distribution for several sideslip angles at an angle of attack of 4° in a take-off configuration. $M_\infty = 0.30$; $\delta_f = 30°$; $\delta_{a,L} = 0°$; *and* $\delta_{a,R} = 0°$.
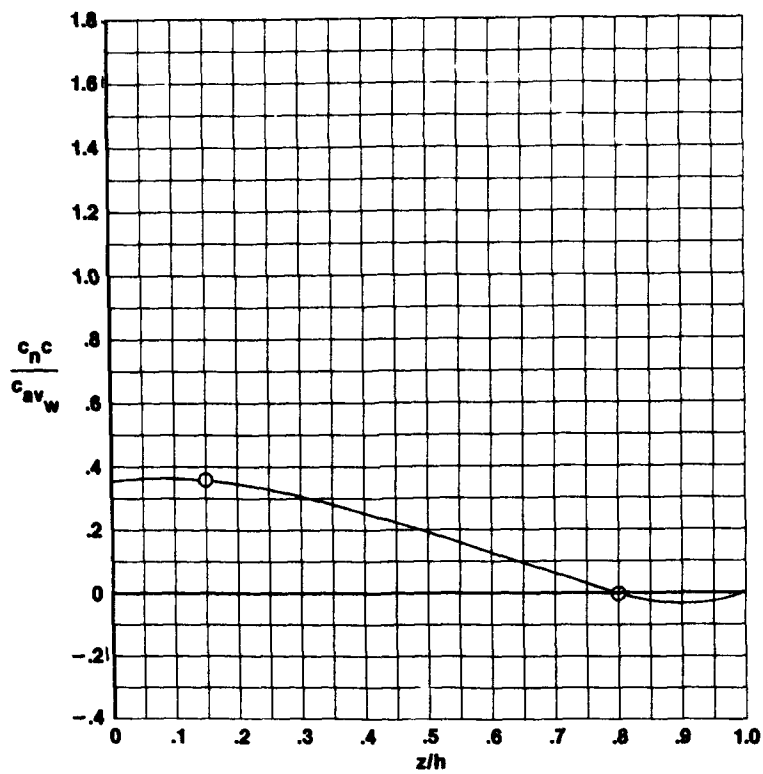
(b) $\alpha = 4.0°$; $\beta = 9.7°$.
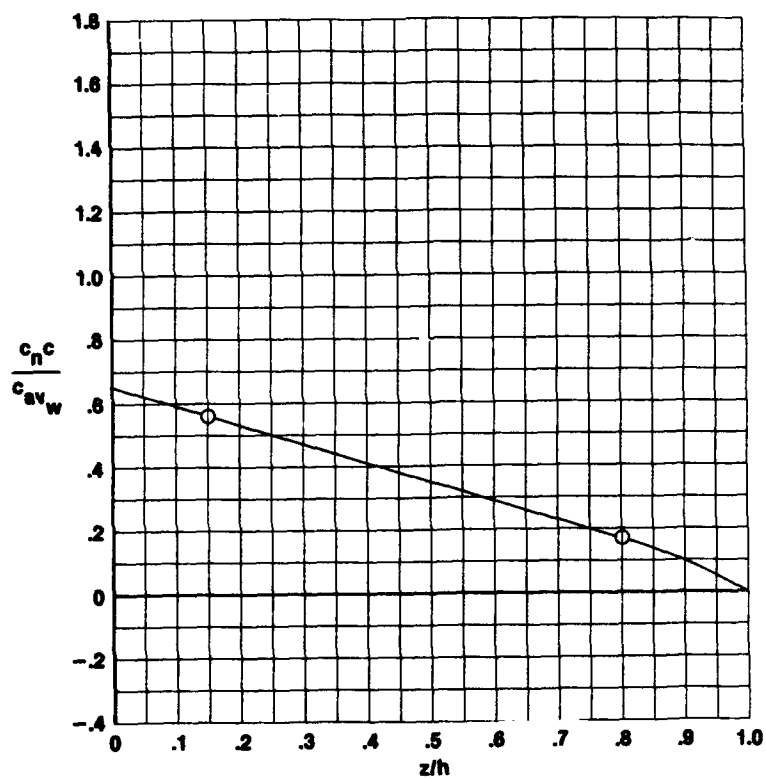
(c) $\alpha = 3.9°$; $\beta = 5.0°$.

Figure 16. Continued.

(d) α = 3.9°; β = 0.2°.
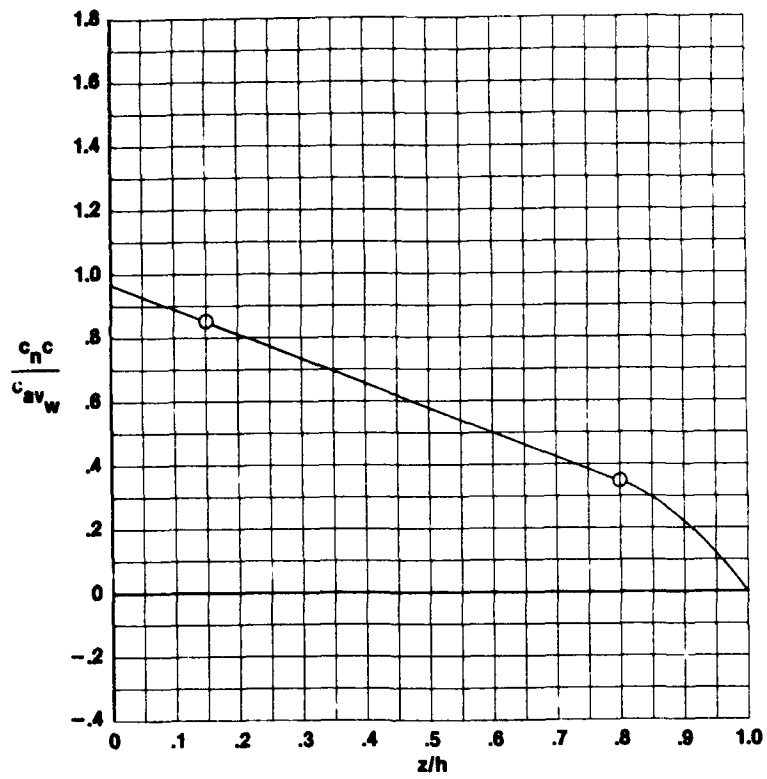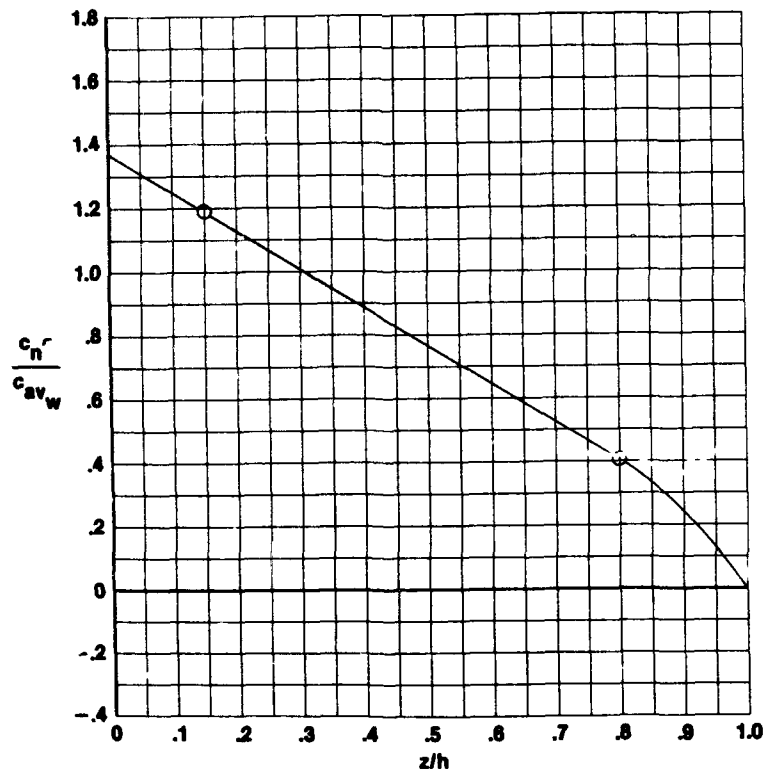
(e) α = 3.9°; β = -5.1°.

Figure 16. Continued.
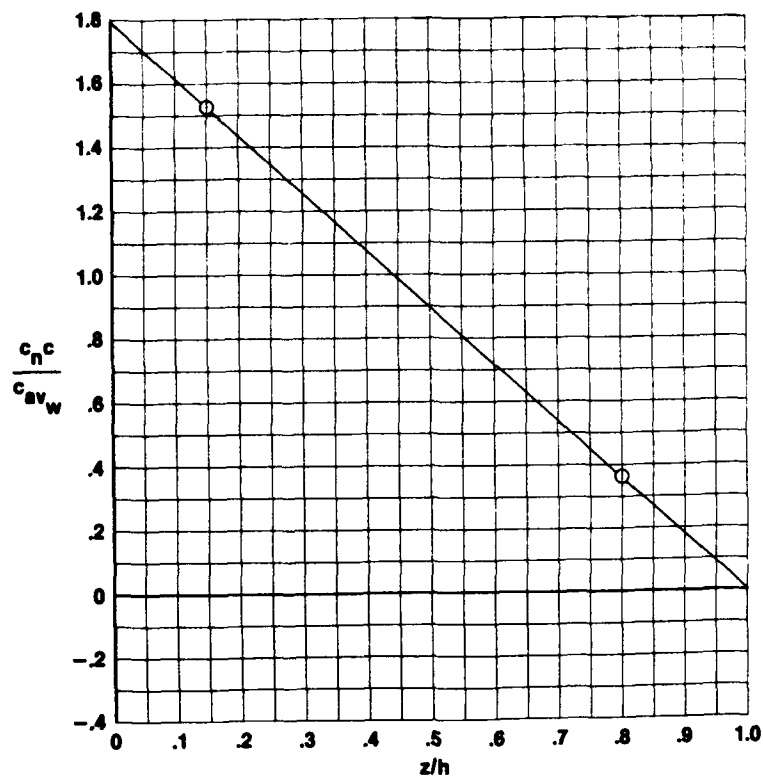
(f) $\alpha = 4.0°$; $\beta = -9.0°$.
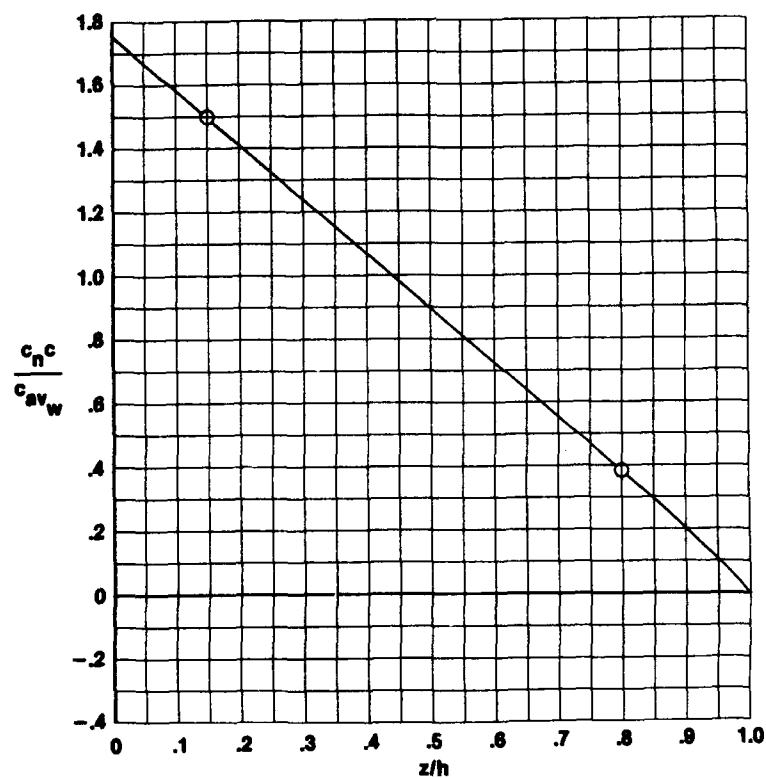
(g) $\alpha = 4.2°$; $\beta = -12.2°$.

Figure 16. Concluded.
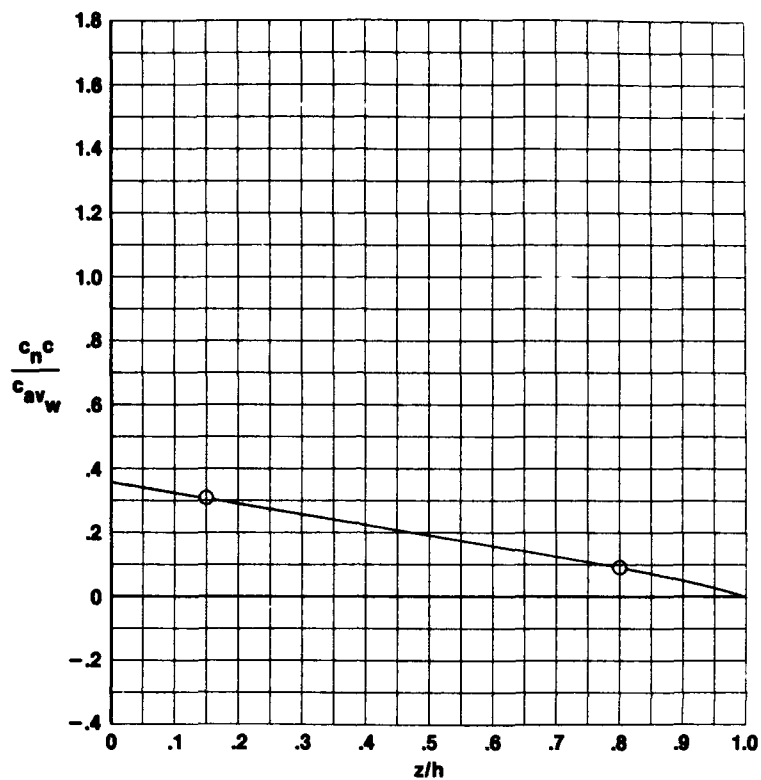
(a) $\alpha = -2.2°$; $\beta = 0°$.

Figure 17. *Variation of left winglet span-
wise load distribution for several angles of
attack at a constant sideslip angle in a
cruise configuration.* $M_\infty = 0.78$.
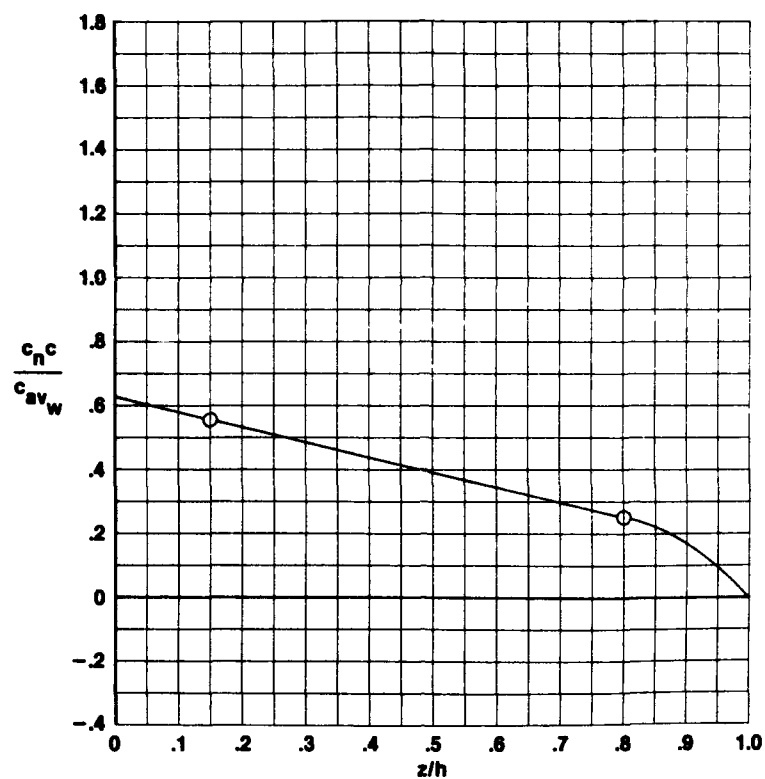
(b) $\alpha = -0.1°$; $\beta = 0°$.
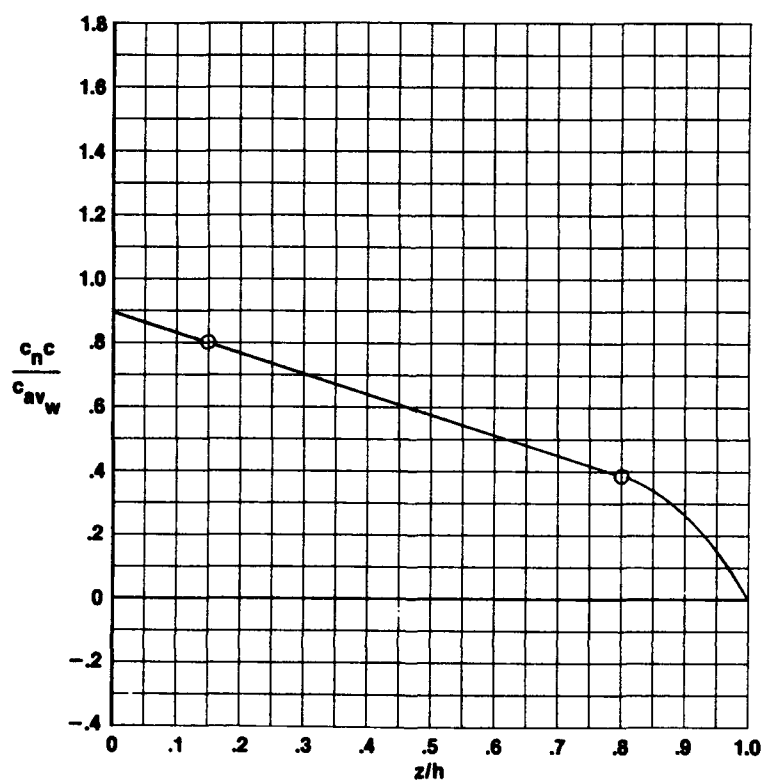
(c) $\alpha = 1.9°$; $\beta = 0°$.

Figure 17. Continued.
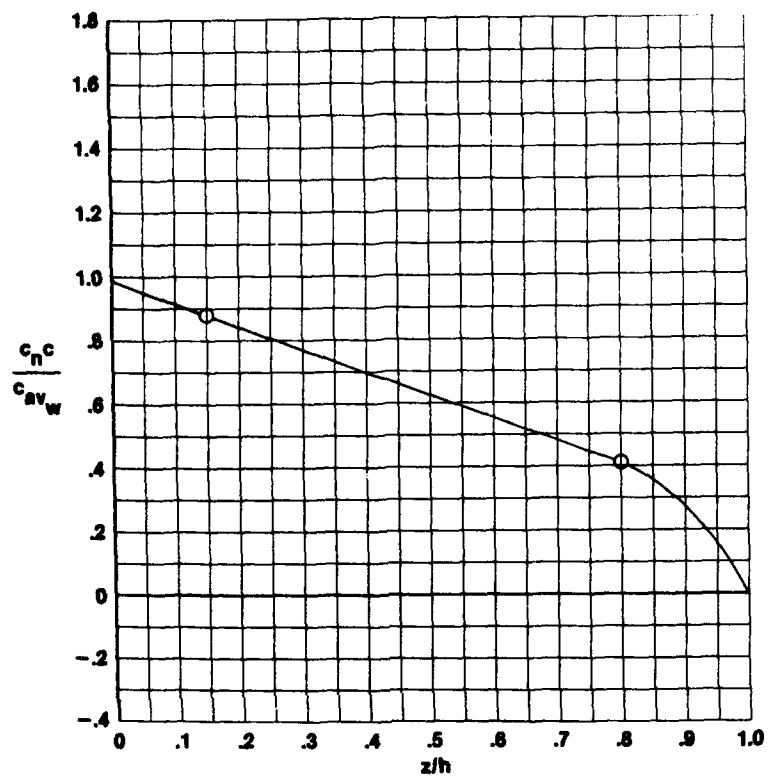
(d) α = 3.9°; β = 0°.

Figure 17. Concluded.
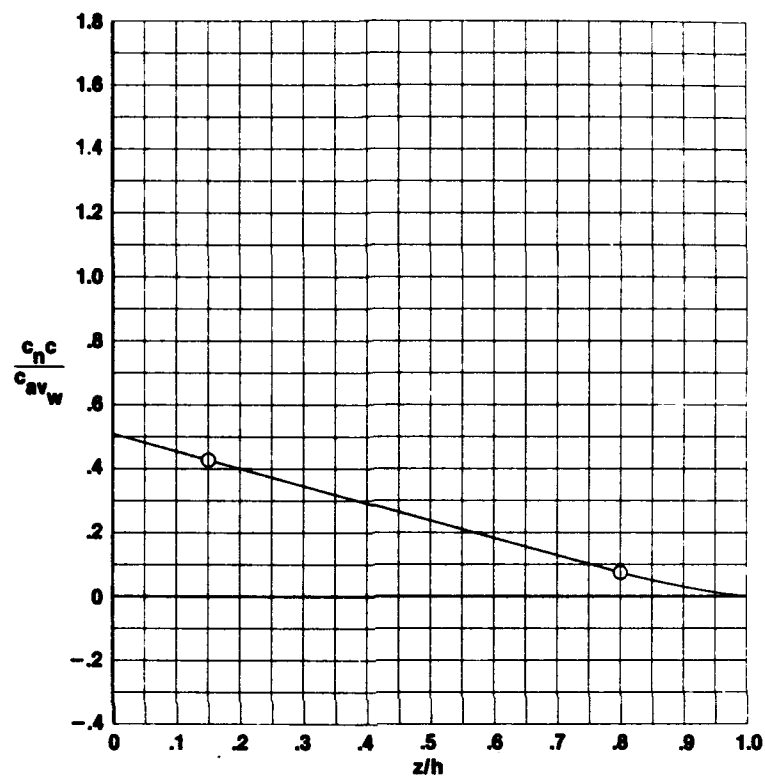
(a) α = 1.9°; β = 5.0°.

Figure 18. Variation of left winglet span-
wise load distribution for several sideslip
angles at a constant angle of attack in a
cruise configuration. M_∞ = 0.78.
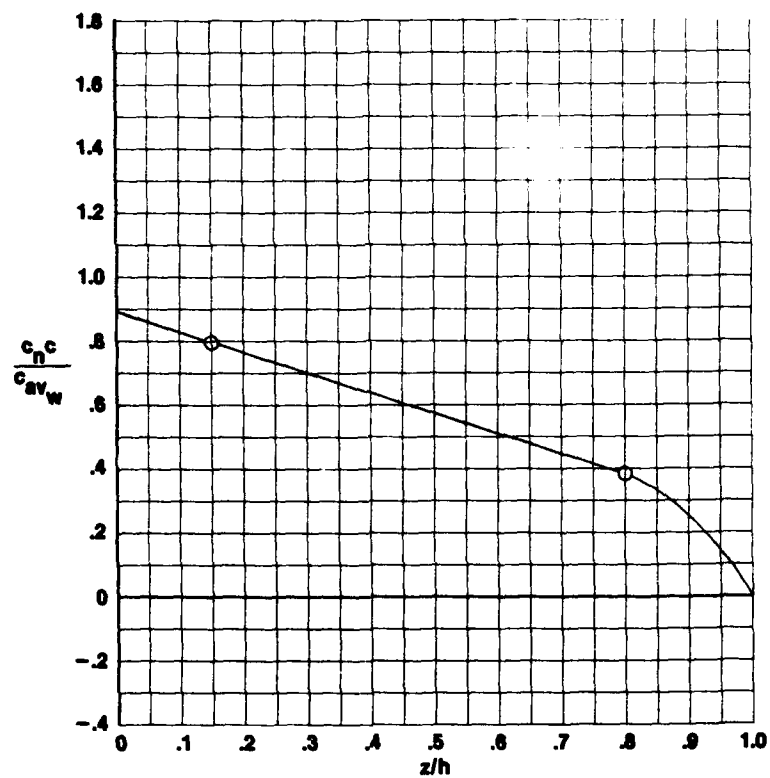
(b) $\alpha = 1.9°$; $\beta = 0°$.
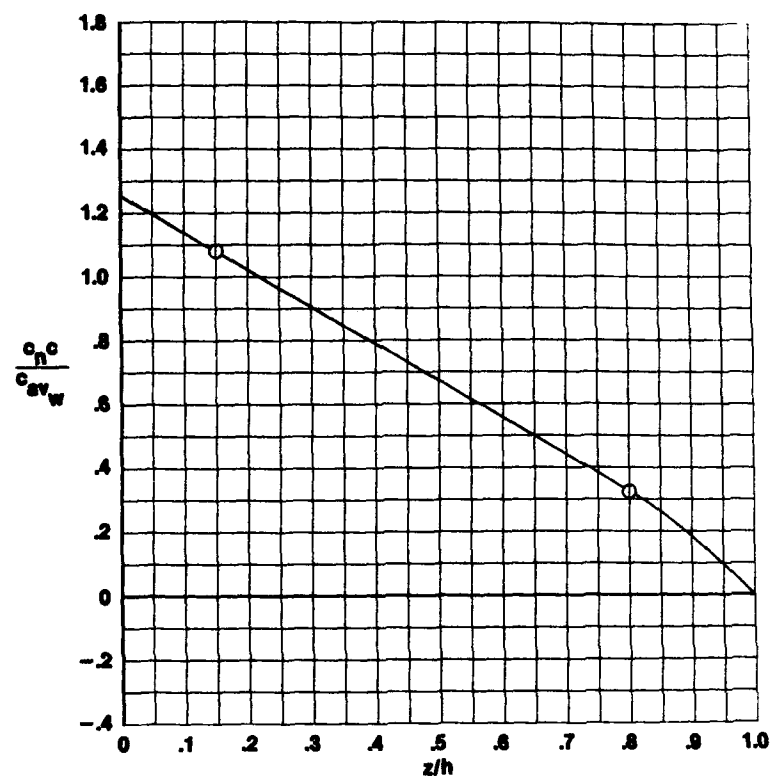
(c) $\alpha = 2.0°$; $\beta = -5.0°$.

Figure 18. Concluded.
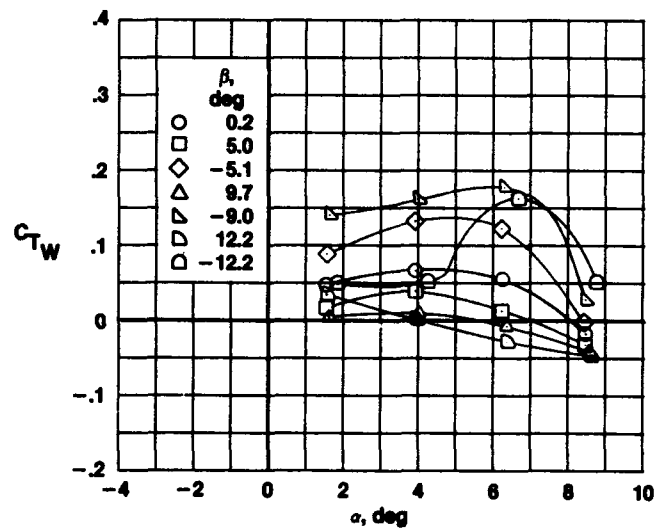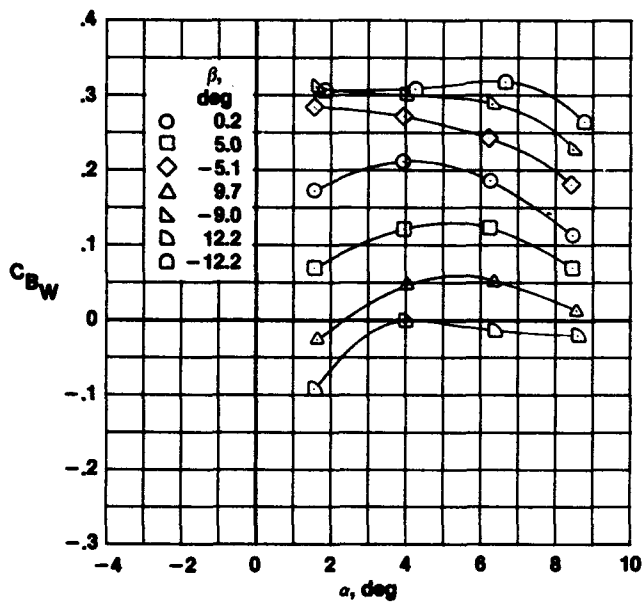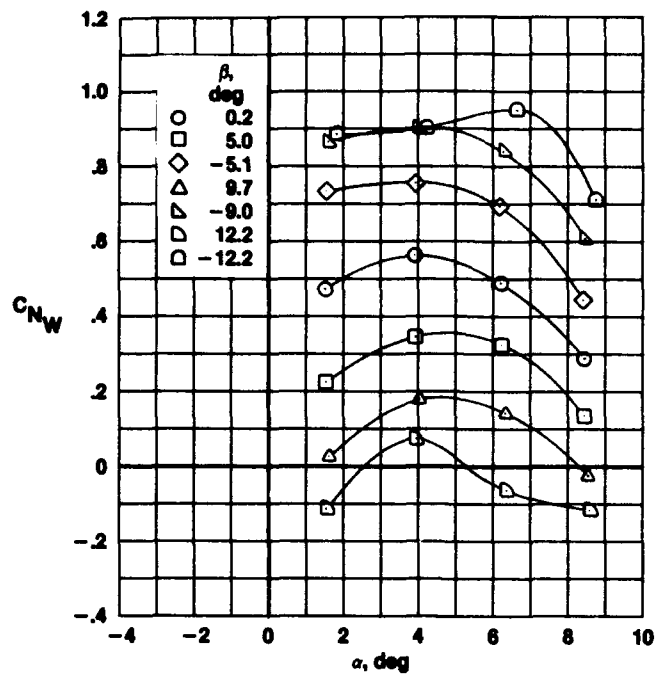
Figure 19. Variation of left winglet loads with angle of attack for several sideslip angles in a takeoff configuration. $M_\infty = 0.30$; $\delta_f = 30°$; $\delta_{a,L} = 0°$; and $\delta_{a,R} = 0°$.
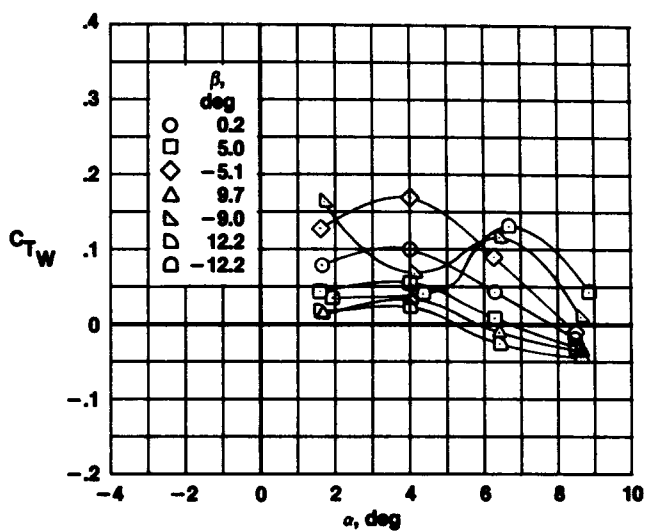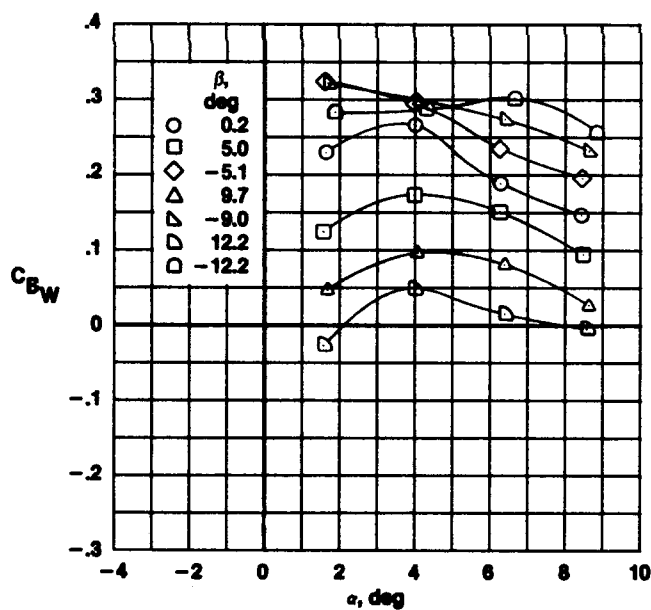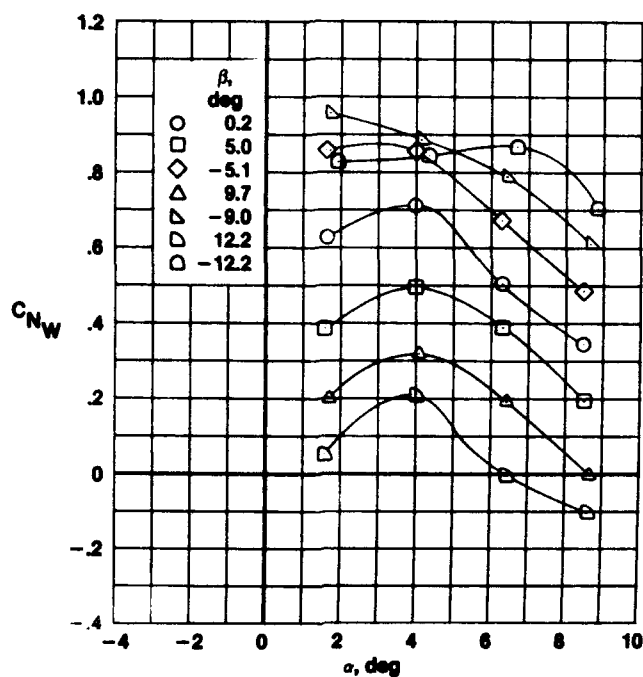
Figure 20. Variation of left winglet loads with angle of attack for several sideslip angles in a takeoff configuration. $M_\infty = 0.30$; $\delta_f = 30°$; $\delta_{a,L} = 20°$; and $\delta_{a,R} = 0°$.
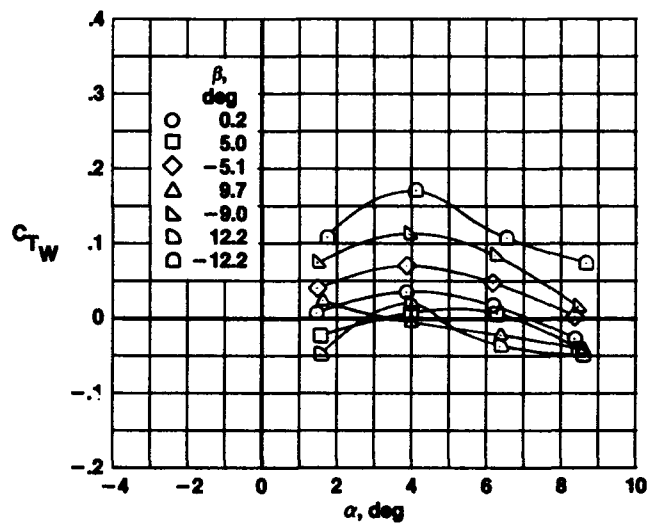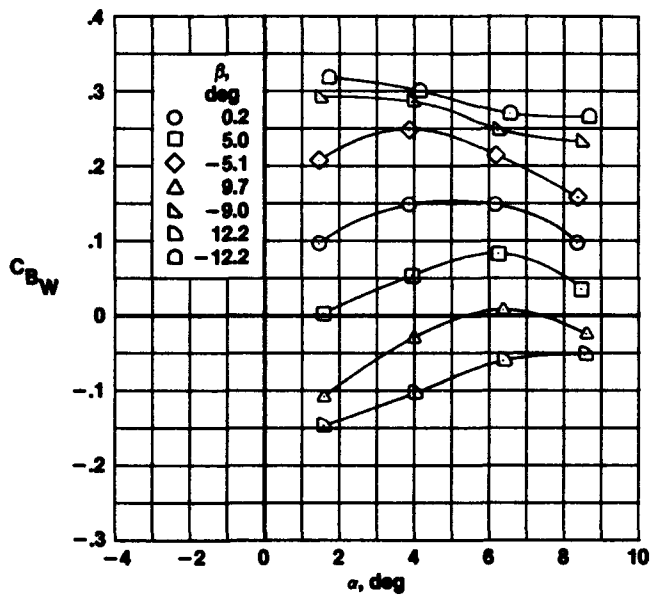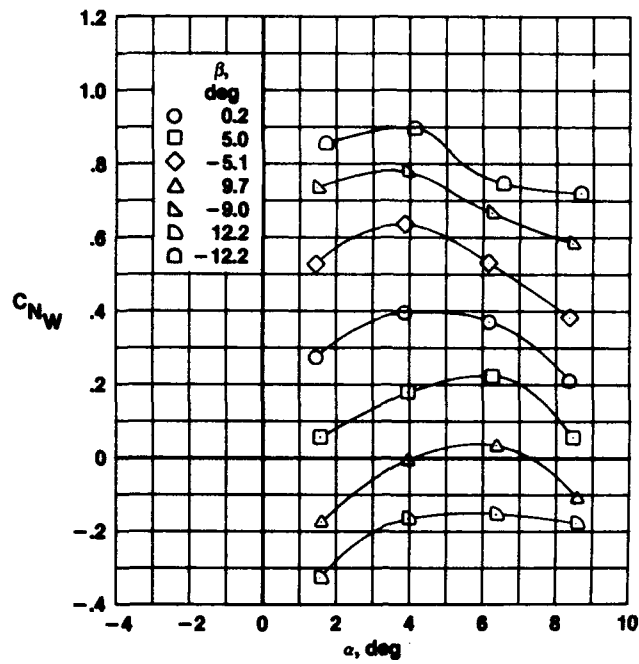
Figure 21. Variation of left winglet loads with angle of attack for several sideslip angles in a takeoff configuration. $M_\infty = 0.30$; $\delta_f = 30°$; $\delta_{a,L} = -20°$; and $\delta_{a,R} = 0°$.
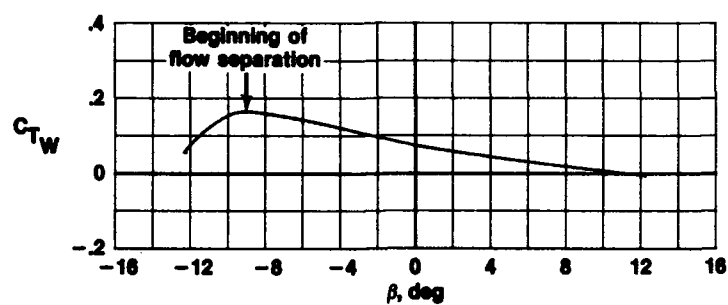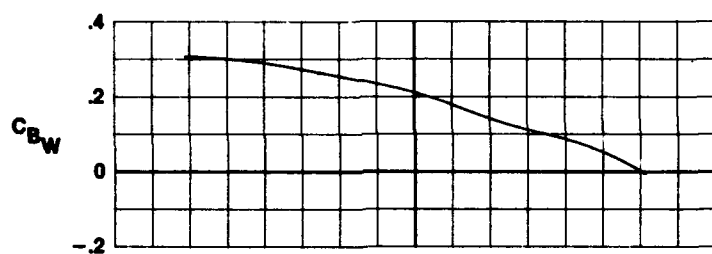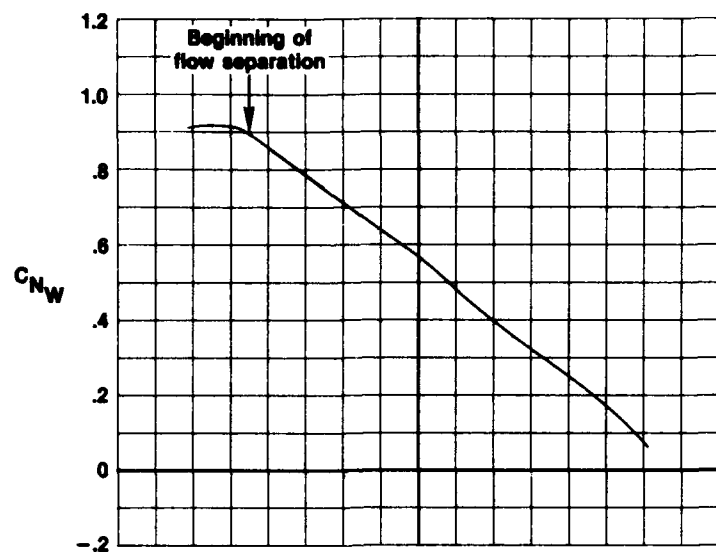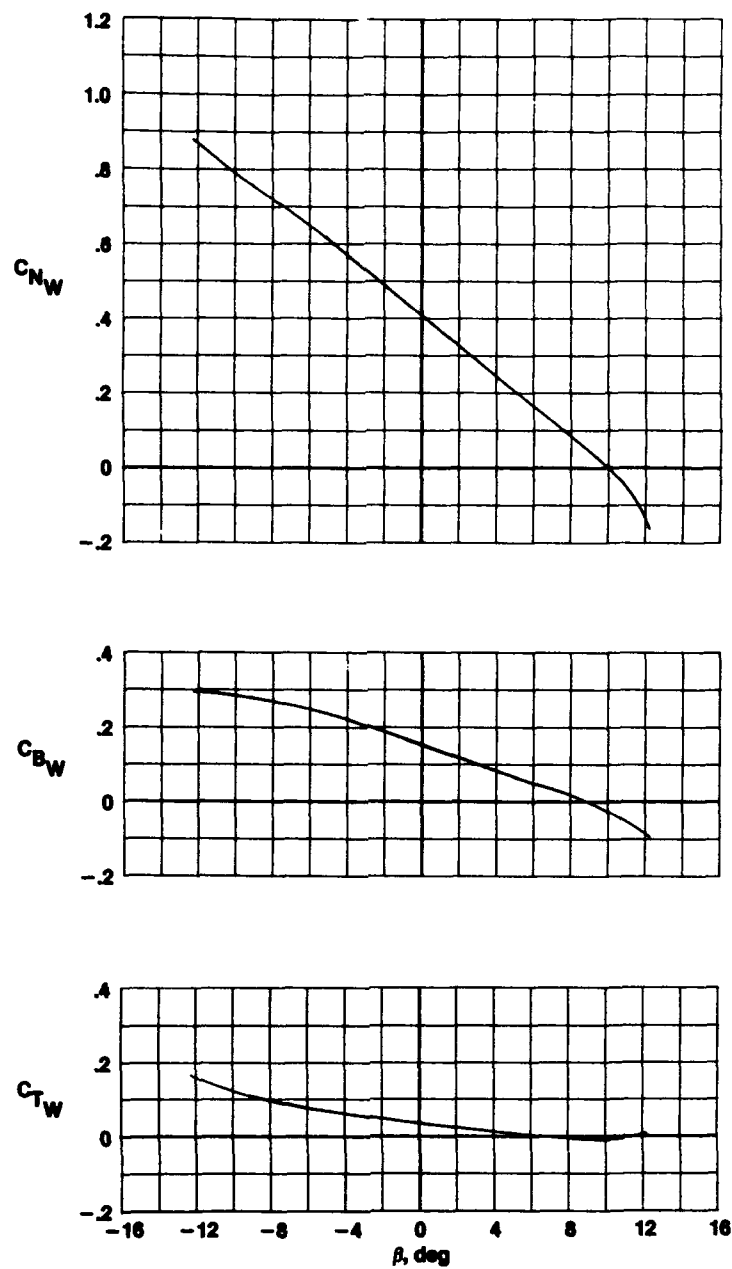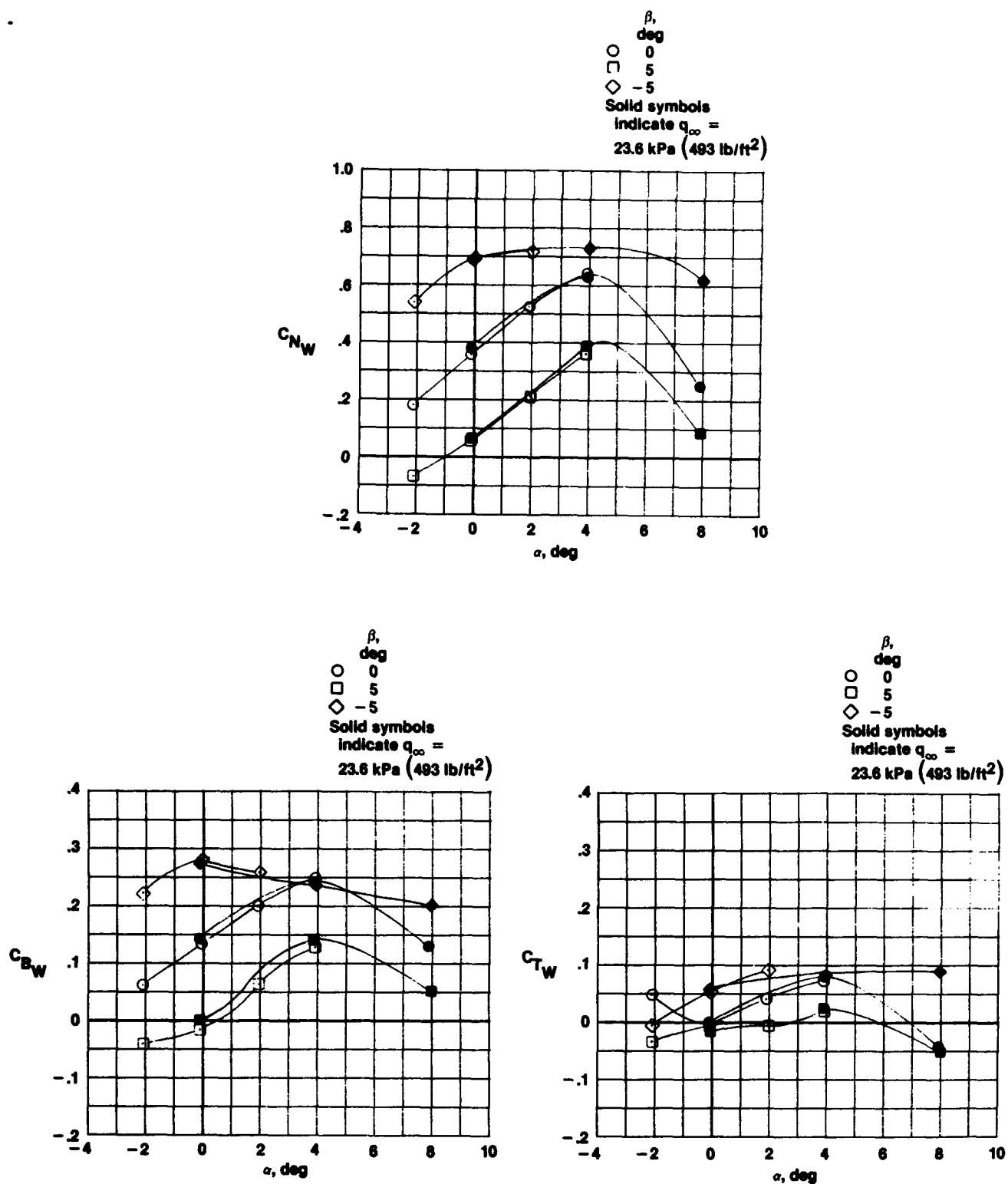
Figure 22. Variation of left winglet loads
with angle of sideslip for an angle of
attack of 4.5° in a takeoff configuration.
$M_\infty = 0.30$; $\delta_f = 30°$; $\delta_{a,L} = 0°$; and
$\delta_{a,R} = 0°$.
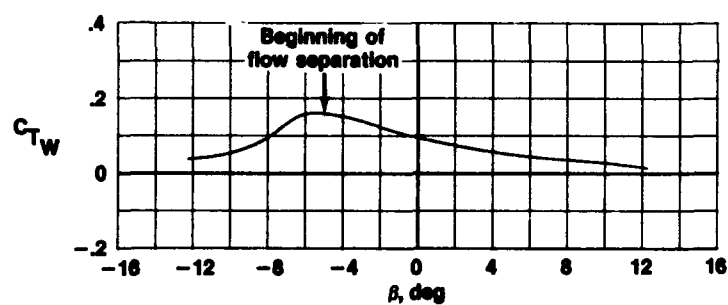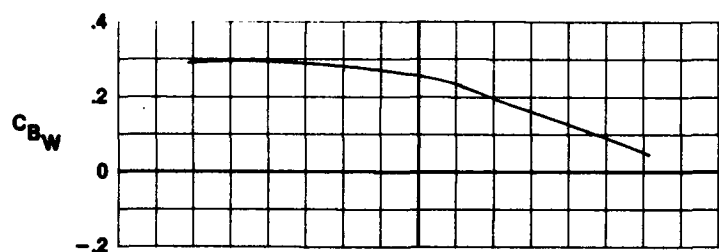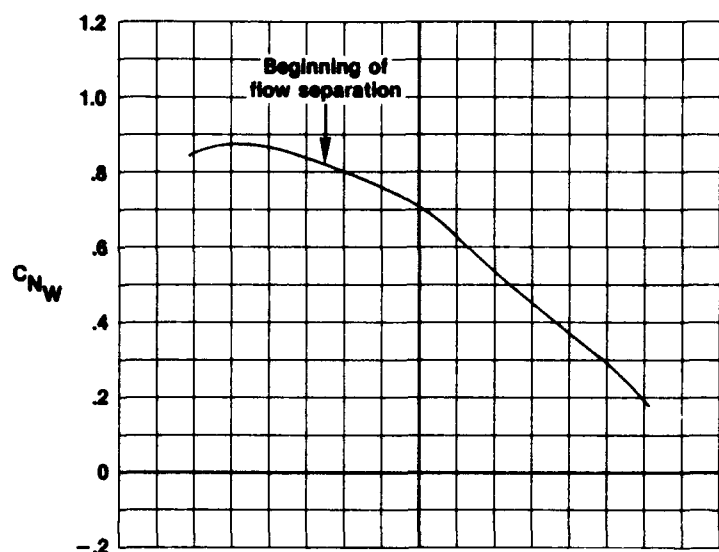
*Figure 23. Variation of left winglet loads
with angle of sideslip for an angle of
attack of 4.5° in a takeoff configuration.*
M_∞ = 0.30; δ_f = 30°; $\delta_{a,L}$ = 20°; $\delta_{a,R}$ = 0°.

Figure 24. Variation of left winglet loads
with angle of sideslip for an angle of
attack of 4.5° in a takeoff configuration.
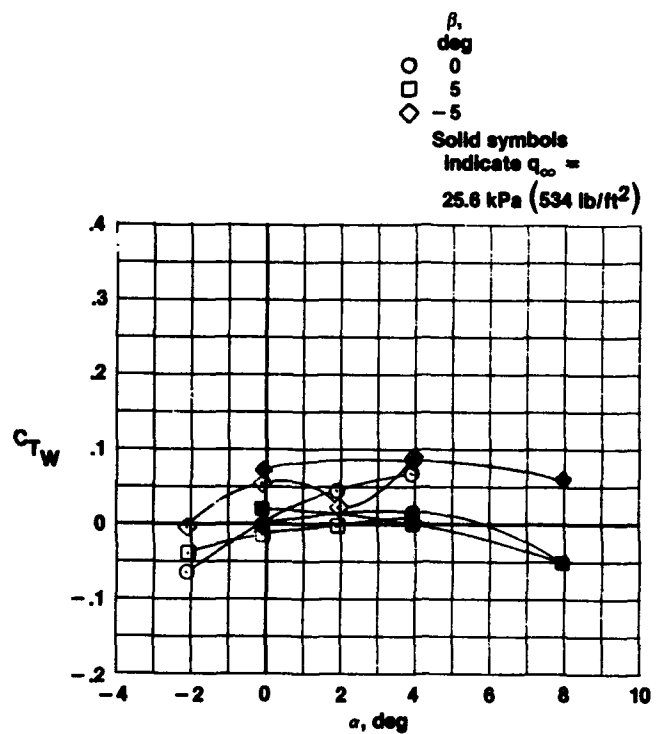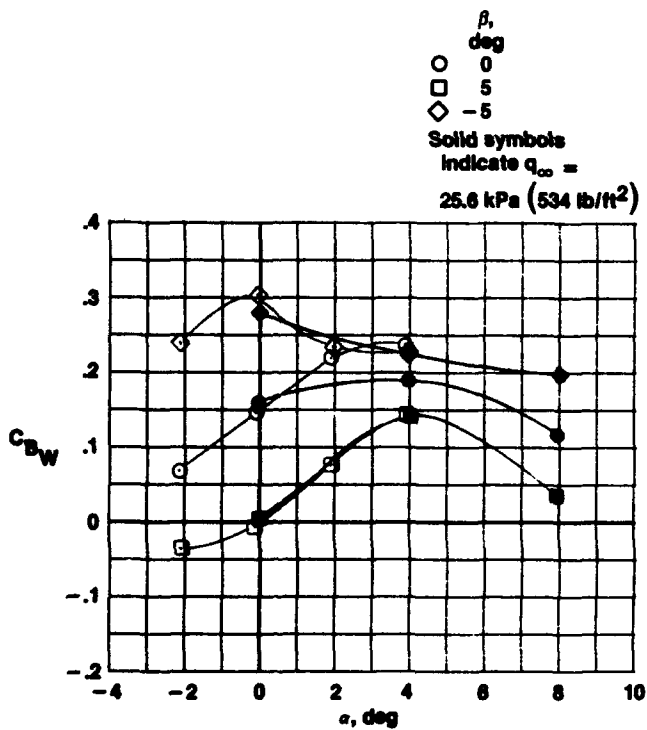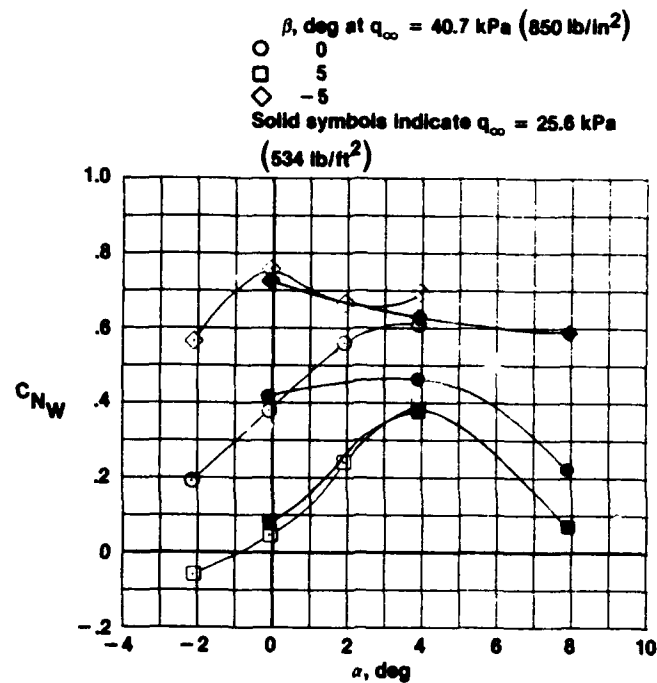$M_\infty = 0.30$; $\delta_f = 30°$; $\delta_{a,L} = -20°$; and
$\delta_{a,R} = 0°$.

Figure 25. Variation of left winglet loads with angle of attack for several sideslip angles in a cruise configuration. $M_\infty = 0.70;$ $q_\infty = 23.6$ kPa (493 lb/ft^2); and $q_\infty = 40.7$ kPa (850 lb/ft^2).

Figure 26. Variation of left winglet loads with angle of attack for several sideslip angles in a cruise configuration. M_∞ = 0.78; q_∞ = 25.6 kPa (534 lb/ft^2); and q_∞ = 40.7 kPa (850 lb/ft^2).
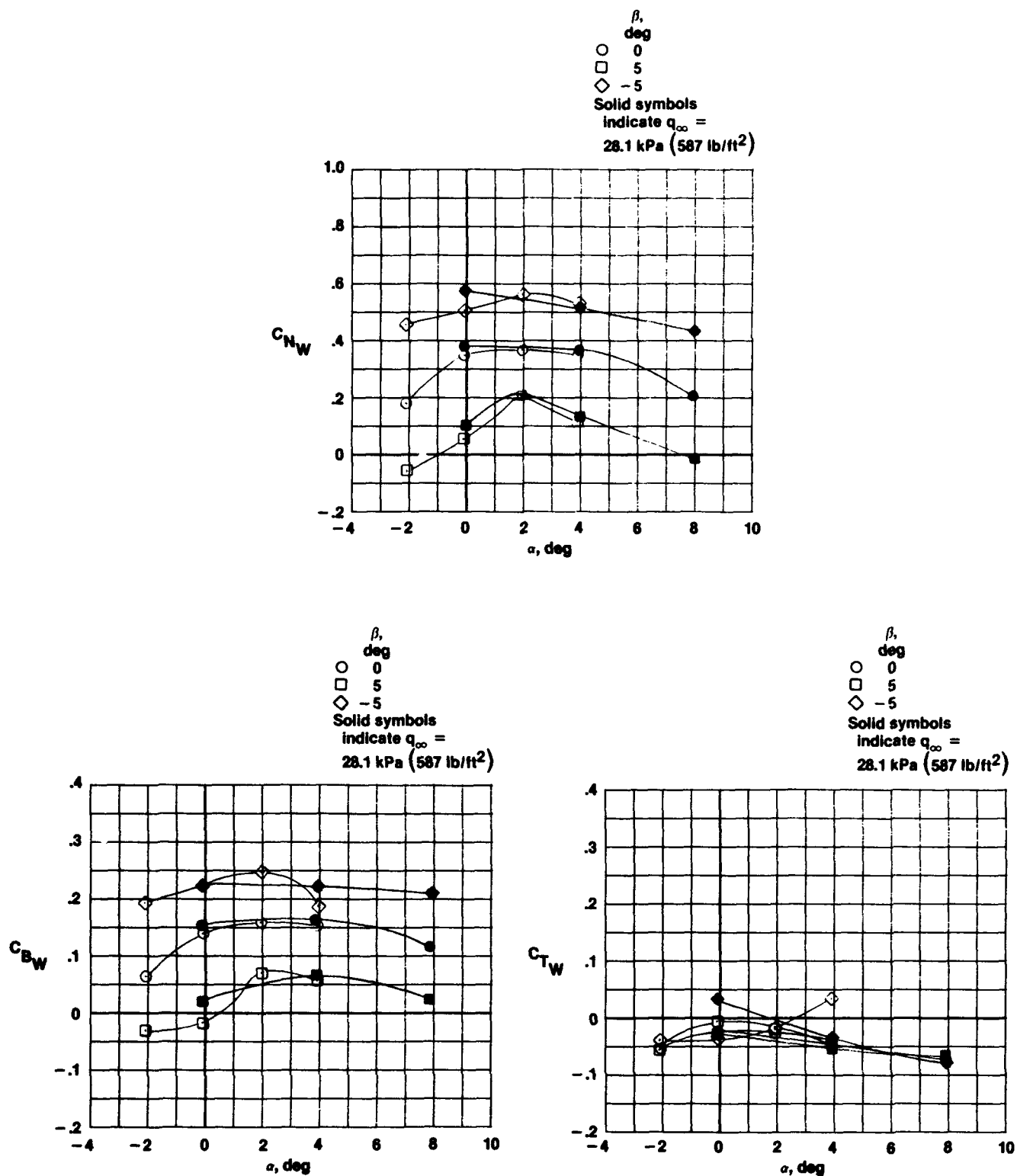
Figure 27. *Variation of left winglet loads with angle of attack for several sideslip angles in a cruise configuration.* $M_\infty = 0.90$; $q_\infty = 28.1$ kPa $(587$ $lb/ft^2)$; *and* $q_\infty = 40.7$ kPa $(850$ $lb/ft^2)$.
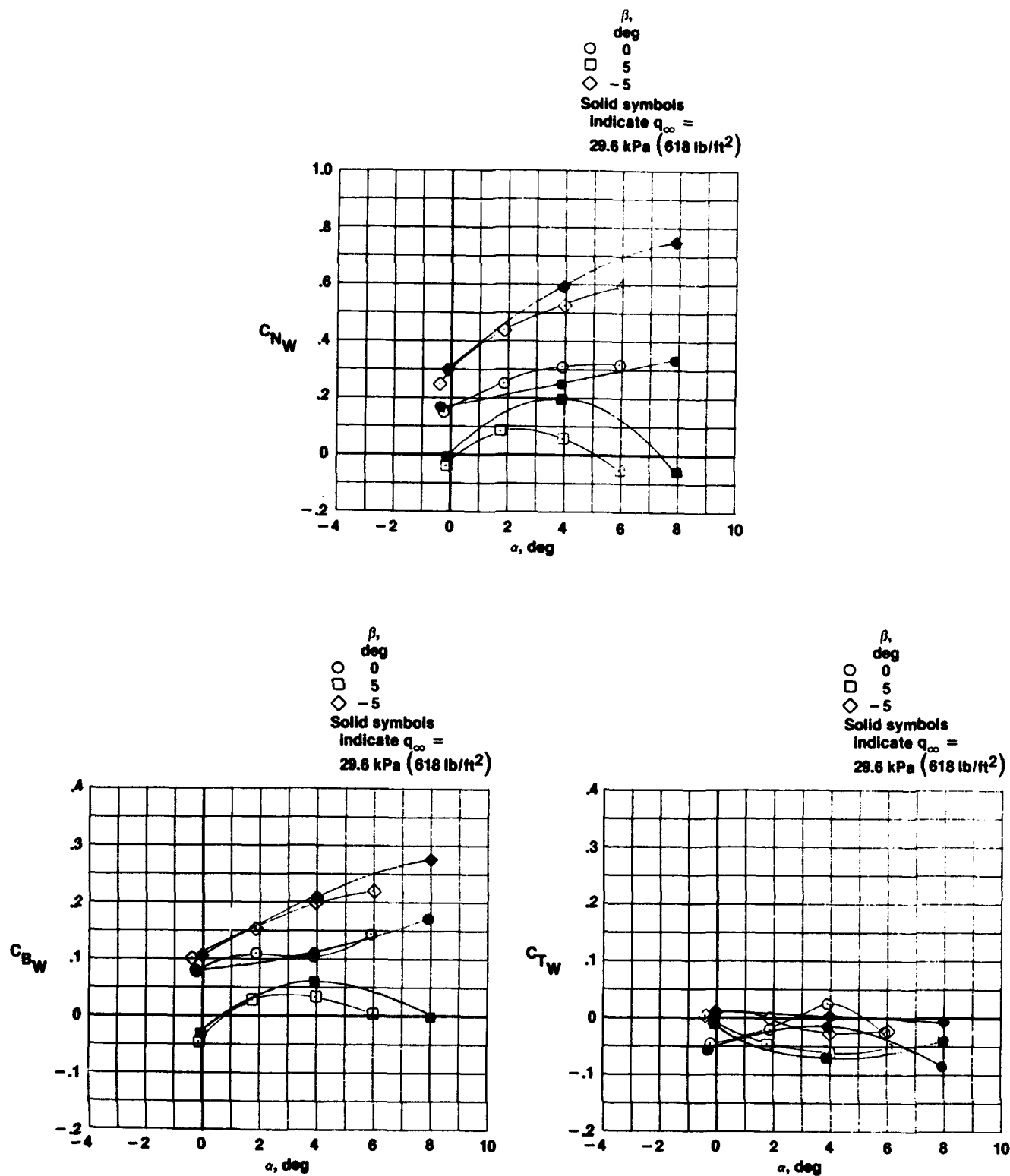
Figure 28. Variation of left winglet loads with angle of attack for several sideslip angles in a cruise configuration. $M_\infty = 0.95$; $q_\infty = 29.6$ kPa $(618 \ lb/ft^2)$; and $q_\infty = 33.8$ kPa $(707 \ lb/ft^2)$.
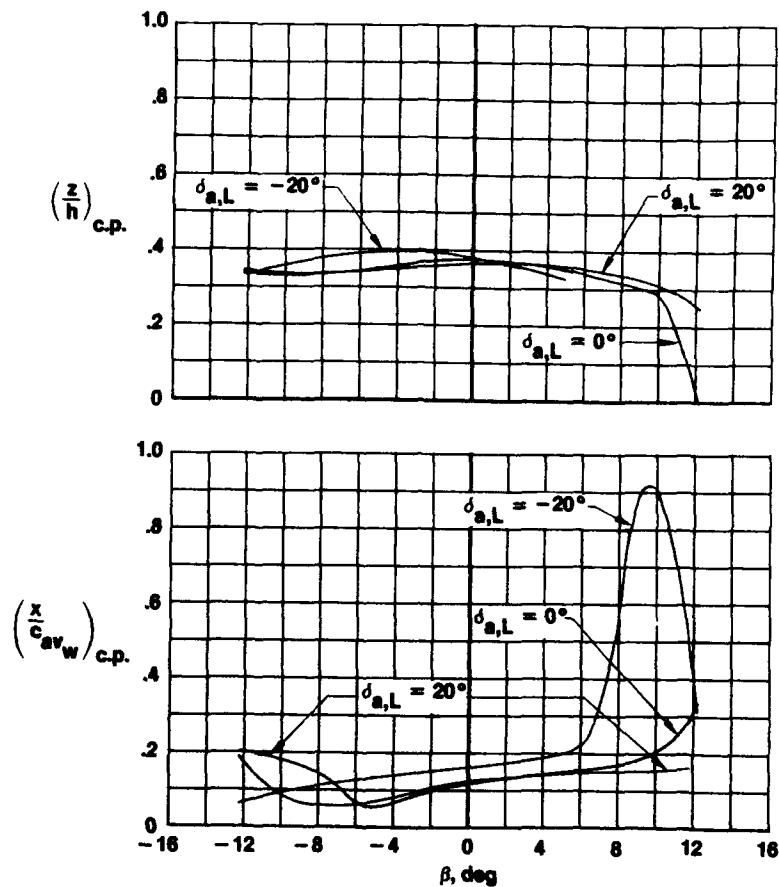
Figure 29. Variation of left winglet center-of-pressure location with angle of sideslip for several aileron deflections in a takeoff configuration. $\alpha = 4.5°$; $M_\infty = 0.30$; $\delta_f = 30°$; and $q_\infty = 40.7$ kPa (850 lb/ft^2).
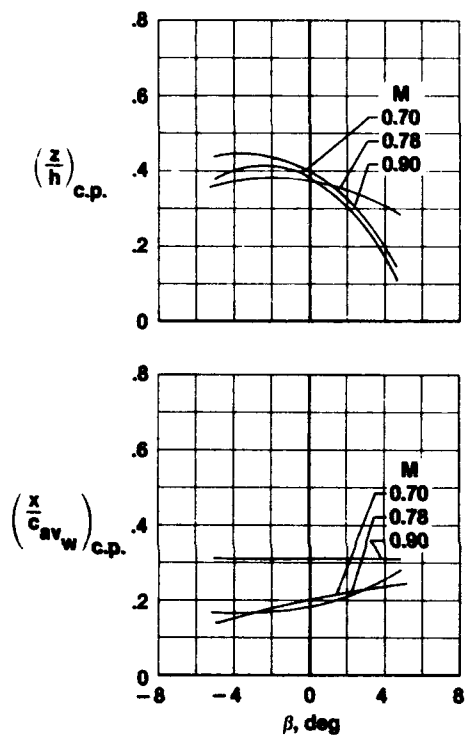
Figure 30. Variation of left winglet center-of-pressure location with angle of sideslip for several Mach numbers in a cruise configuration. $\alpha = 1°$; $q_\infty = 40.7$ kPa (850 lb/ft^2).
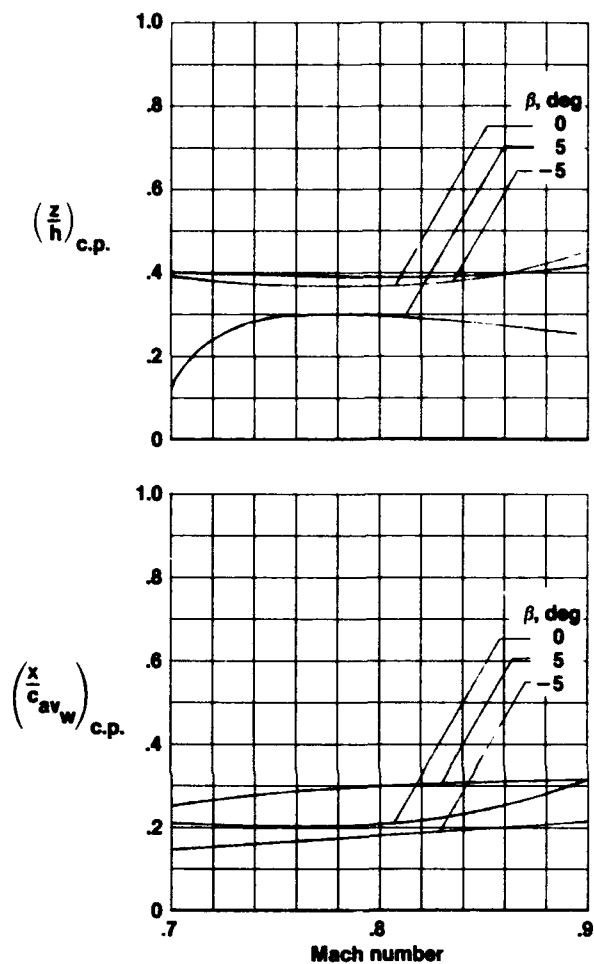
Figure 31. Variation of left winglet center-of-pressure location with Mach number for several angles of sideslip in a cruise configuration. $\alpha = 1°$; $q_\infty = 40.7$ kPa (850 lb/ft^2).

1. Report No. NASA TP-2619	2. Government Accession No.	3. Recipient's Catalog No.
4. Title and Subtitle Effects of Winglets on a First-Generation Jet Transport Wing. VII — Sideslip Effects on Winglet Loads and Selected Wing Loads at Subsonic Speeds for a Full-Span Model		5. Report Date September 1986
		6. Performing Organization Code
7. Author(s) Robert R. Meyer, Jr., and Peter F. Covell		8. Performing Organization Report No. H-1193
		10. Work Unit No.
9. Performing Organization Name and Address NASA Ames Research Center Dryden Flight Research Facility P.O. Box 273 Edwards, California 93523		
		11. Contract or Grant No.
		13. Type of Report and Period Covered Technical Paper
12. Sponsoring Agency Name and Address National Aeronautics and Space Administration Washington, D.C. 20546		
		14. Sponsoring Agency Code RTOP 505-31-21

15. Supplementary Notes

Table 4, "Low-Speed Winglet Pressure Data," and Table 5, "High-Speed Wing and Winglet Pressure Data," are provided in the microfiche supplement (7 sheets total) included in this report.

16. Abstract

The effect of sideslip on winglet loads and selected wing loads was investigated at high and low subsonic Mach numbers. The investigation was conducted in two separate wind tunnel facilities, using two slightly different 0.035-scale full-span models. Results are presented which indicate that, in general, winglet loads as a result of sideslip are analogous to wing loads caused by angle of attack. The center-of-pressure locations on the winglets are somewhat different than might be expected for an analogous wing. The spanwise center of pressure for a winglet tends to be more inboard than for a wing. The most notable chordwise location is a forward center-of-pressure location on the winglet at high sideslip angles. The noted differences between a winglet and an analogous wing are the result of the influence of the wing on the winglet.

17. Key Words (Suggested by Author(s)) Presure distribution Winglet loads Wing loads Sideslip	18. Distribution Statement Unclassified – Unlimited STAR category 02		
19. Security Classif. (of this report) Unclassified	20. Security Classif. (of this page) Unclassified	21. No. of Pages 56	22. Price* A04/E04

*For sale by the National Technical Information Service, Springfield, Virginia 22161.

NASA-Langley, 1986